MODULATION OF THE IMMUNE RESPONSE FOLLOWING PERIPHERAL NERVE INJURY

Ph.D. Thesis

Bernát Nógrádi, M.D.

Supervisors:

László Siklós, Ph.D., D.Sc.

Roland Patai Ph.D.

Laboratory of Neuronal Plasticity, Molecular Neurobiology Research Unit, Institute of Biophysics, Biological Research Centre, Szeged, Hungary

Doctoral School of Theoretical Medicine, University of Szeged, Hungary

Department of Neurology, University of Szeged, Hungary

Szeged

2022

“I think life on Earth must be about more than just solving problems...

It's got to be something inspiring, even if it is vicarious.”

Elon Musk

List of publications

Publications related to the subject of the thesis

I. Molnár K*, **Nógrádi B***, Kristóf R, Mészáros Á, Pajer K, Siklós L, et al. Motoneuronal inflammasome activation triggers excessive neuroinflammation and impedes regeneration after sciatic nerve injury. J Neuroinflammation. 2022;19(1):268. (IF (2021): 9.594, Journal Ranking: D1)

II. **Nógrádi B***, Nyúl-Tóth Á*, Kozma M, Molnár K, Patai R, Siklós L, et al. Upregulation of nucleotide-binding oligomerization domain-, LRR- and pyrin domain-containing protein 3 in motoneurons following peripheral nerve injury in mice. Front Pharmacol. 2020;11:584184. (IF (2020): 5.811, Journal Ranking: Q1)

III. **Nógrádi B,** Meszlényi V, Patai R, Polgár TF, Spisák K, Kristóf R, at al. Diazoxide blocks or reduces microgliosis when applied prior or subsequent to motor neuron injury in mice. Brain Res. 2020;1741:146875. (IF (2020): 3.252, Journal Ranking: Q2)

***** = The authors contributed equally and share first authorship.

Publications not included in the thesis

I. Polgár TF, Meszlényi V, **Nógrádi B**, Körmöczy L, Spisák K, Tripolszki K, et al. Passive transfer of blood sera from ALS patients with identified mutations results in elevated motoneuronal calcium level and loss of motor neurons in the spinal cord of mice. Int J Mol Sci. 2021;22(18):9994. (IF (2021): 6.208, Journal Ranking: D1)

II. Mészáros Á, Molnár K, **Nógrádi B**, Hernádi Zs, Nyúl-Tóth Á, Wilhelm I, et al. Neurovascular inflammaging in health and disease. Cells. 2020;9(7):1614. (IF (2020): 6.600, Journal Ranking: Q1)

III. Meszlényi V, Patai R, Polgár TF, **Nógrádi B**, Körmöczy L, Kristóf R, et al. Passive transfer of sera from ALS patients with identified mutations evokes an increased synaptic vesicle number and elevation of calcium levels in motor axon terminals, similar to sera from sporadic patients. Int J Mol Sci. 2020;21(15):5566. (IF (2020): 5.924, Journal Ranking: D1)

IV. Obál I, **Nógrádi B**, Meszlényi V, Patai R, Ricken G, Kovacs GG, et al. Experimental motor neuron disease induced in mice with long-term repeated intraperitoneal injections of serum from ALS patients. Int J Mol Sci. 2019;20(10):2573. (IF (2019): 4.556, Journal Ranking: Q1)

V. Meszlényi V, Patai R, **Nógrádi B**, Engelhardt JI, Siklós L. Commentary: Calcium in the pathomechanism of amyotrophic lateral sclerosis – Taking center stage? J Neurol Neuromed. 2017;2(4):1-4. (Journal is not indexed by Clarivate JCR.)

VI. Patai R, **Nógrádi B**, Meszlényi V, Obál I, Engelhardt JI, Siklós L. Az amyotrophiás lateralsclerosis patofiziológiai tényezőinek központi kapcsolóeleme, a kálcium. Ideggyogy Szemle. 2017;70(7-8):247-257. (IF (2017): 0.252, Journal Ranking: Q4)

VII. Patai R, **Nógrádi B**, Engelhardt JI, Siklós L. Calcium in the pathomechanism of amyotrophic lateral sclerosis - Taking center stage? Biochem Biophys Res Commun. 2017;483(4):1031-1039. (IF (2017): 2.559, Journal Ranking: Q1)

Table of contents

List of publications 1
List of abbreviations 5
Introduction 8
Injuries of the peripheral nervous system 8
Peripheral nerve reconstruction 9
Targeting neuroinflammation after acute nerve injury 9
Early components of the inflammasome pathway 10
The NLRP3 inflammasome cascade as a drug target 11
Aims 13
Methods 14
Experimental animals, surgical interventions, and pharmacological treatments 14
Immunohistochemistry (IHC) and immunofluorescent (IF) staining and imaging 16
Quantification of the NLRP3, microglia and astroglia staining 19
Morphological analysis of microglial cells after hypoglossal axotomy 20
Quantification of motoneuronal survival after hypoglossal axotomy 20
Tissue preparation for electron microscopy and analysis of mitochondrial morphometry 21
Tissue preparation and western blot 21
Sciatic functional index (SFI) measurements 22
Retrograde labeling experiments after sciatic axotomy 23
Statistical analysis 23
Results 24
NLRP3 expression in the hypoglossal and oculomotor nucleus following axotomy 24
Subcellular distribution of NLRP3 and inflammasome activation following hypoglossal axotomy 28
Effect of diazoxide on NLRP3 expression after hypoglossal nerve axotomy 32
Effect of diazoxide on ramification and activation of microglial cells after hypoglossal axotomy 33
Effect of diazoxide on motoneuronal survival and mitochondrial morphology 35
NLRP3 expression in the spinal cord, dorsal root ganglion and sciatic nerve following sciatic nerve axotomy 38
Effect of NLRP3 inhibition on the microgliosis and astrogliosis in the spinal cord after sciatic nerve axotomy 42
Inhibition of inflammasome activation promotes neural regeneration 46
Discussion 52
Summary 56

Bibliography 58
Acknowledgements 69
Appendix 70

List of abbreviations

a.u.	arbitrary unit
AIM2	absent in melanoma 2
ALS	amyotrophic lateral sclerosis
AQP4	aquaporin-4
ASC	apoptosis-associated speck-like protein containing a caspase-recruitment domain
Ax.	axotomy
BCA	bicinchoninic acid assay
BSA	bovine serum albumin
CH	convex hull
ChAT	choline acetyltransferase
CNS	central nervous system
Coapt.	axotomy + coaptation
DAB	diaminobenzidine tetrahydrochloride
DAMP	damage-associated molecular pattern
DMSO	dimethyl-sulfoxide
DRG	dorsal root ganglion
DZX	diazoxide
eATP	extracellular ATP
EPL	experimental paw length
ETS	experimental toe spread
FB	fast blue
GFAP	glial fibrillary acidic protein
HMGB1	high mobility group box 1

Iba1	ionized calcium-binding adaptor molecule 1
IF	immunofluorescent
IFI16	interferon gamma-inducible protein 16
IHC	immunohistochemistry
IL-18	interleukin-18
IL-1β	interleukin-1 beta
mtDNA	mitochondrial DNA
n.s.	non-significant
NEFM	neurofilament medium polypeptide
NeuN	neuronal nuclei protein
NF-κB	nuclear factor kappa-light-chain-enhancer of activated B cells
NLRA	nucleotide-binding oligomerization domain and leucine-rich repeat receptors family acidic transactivating domain
NLRP	nucleotide-binding oligomerization domain-, leucine-rich repeat- and pyrin domain-containing proteins
NPL	normal paw length
NSAID	non-steroid anti-inflammatory drug
NTS	normal toe spread
p75	p75 neurotrophin receptor
PBS	phosphate buffered saline
PFA	paraformaldehyde
PNI	peripheral nerve injury
PNS	peripheral nervous system
PRR	pattern recognition receptors
PVDF	polyvinylidene difluoride membranes

ROS	reactive oxygen species
SCI	spinal cord injury
SEM	standard error of the mean
SFI	sciatic functional index
STED	stimulated emission depletion
TBI	traumatic brain injury
TBS-T	tris-buffered saline with 0.1 % Tween-20
TPBS	10 mM PBS containing 0.2 % Triton X-100
TRPV1	transient receptor potential vanilloid 1
WB	western blot

Introduction

Injuries of the peripheral nervous system

Acute injuries of the peripheral nervous system (PNS) are relatively common, with a yearly incidence of 3.69-13.9 per 100 000 [1,2]. Peripheral nerve injuries (PNI) often occur in young individuals and among the most common causes are trauma, surgery, chemotherapy, radiation therapy and birth complications [3]. While PNS injuries are mostly not life-threatening conditions, they can result in a significant decline in the quality of life, especially when the reinnervation of muscles is delayed, leading to muscle atrophy and permanent loss of function [3]. Also, more than half of patients who underwent surgical procedure following acute nerve injury reported chronic pain [4], the incidence of which increases with age [5]. The relatively high incidence rate of PNI, its manifestation amongst young adults, the high risk of incomplete recovery and the potential complications lead to a substantial socio-economic burden, *e.g.*, 30 % of the patients reported permanent disability after peripheral nerve injury of the upper extremity, as reported by Bergmeister *et al.* [6].

Peripheral nerve injuries can be classified based on the mechanism of injury (compression, crush, transection, etc.), however, a more commonly used classification system was created by Seddon [7] and later extended by Sunderland [8], which is based on the severity of the nerve damage. Based on this, the mildest form of PNS injury is neuropraxia (Seddon classification) or grade I injury (Sunderland classification), which is a focal segmental demyelination of the nerve, usually caused by mild compression. Moderate injuries fall into the category of axonotmesis (Seddon) or grade II-IV injuries (Sunderland), where the injury results in direct axonal damage, but the continuity of the axons is preserved. The most severe form of nerve injury, neurotmesis (Seddon) or grade V-VI injuries cover the complete transection of the nerve. Unsurprisingly, the potential regenerative outcome greatly depends on the severity of the injury [9].

When compared to acute injuries of the central nervous system (CNS), PNS injuries are generally associated with a better functional outcome due to the differences in their regenerative capabilities, *i.e.*, axonal regeneration is extremely limited in the CNS; while axons readily regenerate in the PNS [10,11]. A variety of different factors have been identified which contribute to the increased regenerative potential of the PNS, including differences in gene expression, growth-promoting microenvironment, enhanced debris clearance and inflammatory reaction. Despite this permissive growth environment, the functional recovery after peripheral nerve injury is often suboptimal. As peripheral nerve growth occurs at a relatively slow rate of

1 mm per day in humans, regeneration and reinnervation can take up to 3-6 months [9]. The injured axons eventually lose their regenerative capabilities in a progressive manner, depending on the time and axonal distance necessary for complete regrowth [12,13], which often results in delayed and incomplete recovery.

Peripheral nerve reconstruction

The currently accepted clinical therapy for peripheral nerve injury is surgical reconstruction. Direct nerve repair with epineural sutures and tension-free coaptation technique is mostly used for severe axonotmesis and neurotmesis injuries. When direct repair would result in excessive tension due to the gap between the nerve endings, the use of autologous nerve grafts is required [14]. It is noteworthy, that autologous nerve grafts undergo Wallerian degeneration, thus they merely provide mechanical guidance for the regrowing axons. However, several different factors limit the success rate of reconstructive surgeries, including delayed repair, technical limitations, poor local vasculature and limited availability of sensory allografts [15]. Even though such surgical approaches enable axonal regeneration through the restoration of supporting structures, they have limited effect on the acceleration of nerve regrowth speed. Since this is considered to be a crucial limiting factor for complete recovery, most pharmaceutical approaches aim to accelerate axonal regeneration by modulation of the nerve's microenvironment, in order to improve the functional outcome.

Multiple therapeutic interventions were proven to be beneficial and improve nerve regeneration in rodents, however, these have not yet translated into clinically applicable therapies [11], thus the need for novel high-efficacy therapies is increasingly relevant in acute nerve injury.

Targeting neuroinflammation after acute nerve injury

In traumatic PNI scenarios, the initial mechanic injury of the nerve and the surrounding tissues is considered as the primary injury, which is followed by the so-called secondary injury, *i.e.*, a combination of pathophysiological processes induced by the acute primary insult. Even though the pathomechanism of acute PNS injury is complex and multifaceted [9], neuroinflammation takes central role in the secondary injury mechanisms following acute nerve injury [16,17]. Injuries of the PNS induce a process named Wallerian degeneration, which includes the disintegration of injured axons distal to the site of the lesion [18]. Wallerian degeneration prompts activation of both pro- and anti-inflammatory pathways, necessary for macrophage recruitment and myelin phagocytosis [19]. PNS injuries also trigger neuroinflammatory reactions around the axotomized neuronal cell somas in the spinal cord and dorsal root ganglia

[20], however, there is no general consensus on how this affects the functional outcome. While injury-induced inflammation might have both beneficial and detrimental aspects [21–23], overactivation of pro-inflammatory pathways can negatively influence the regenerative outcome [24,25]. Therefore, it is generally viewed as a promising point of intervention to alleviate secondary injury in PNS. Unsurprisingly, a number of therapeutic experiments have targeted neuroinflammation in the past in both acute CNS and PNS injury scenarios, however, their effectiveness varied and showed inconsistencies [26]. Consequently, their use is not widely supported and lacks higher level evidence to date. Dexamethasone, a commonly used glucocorticoid valued for its anti-inflammatory properties, could only reduce microglial activation in traumatic brain injury (TBI) models, if it was administered immediately after the injury [26]. In peripheral nerve injury, the use of dexamethasone is debated due to its neurotoxic properties [27], although it could improve the functional outcome following sciatic nerve crush when combined with erythropoietin [28]. The potential beneficial therapeutic effects of numerous non-steroid anti-inflammatory drugs (NSAIDs) (ibuprofen, indomethacin, nimesulide) were also evaluated in TBI models, and even though certain studies confirmed the reduction of pro-inflammatory factors, they had no significant effect on the functional outcome [26]. In a tibial nerve transection model, the beneficial effect of ibuprofen on the functional outcome and remyelination has been documented in rats [29], although this has not been further investigated. The pro-regenerative effects of additional anti-inflammatory agents, such as tumor necrosis factor inhibitors, interleukin-1 inhibitors and phosphodiesterase inhibitors have also been investigated. In these studies, the general conclusion was that most of these substances can either not exert a neuroprotective effect or can only do so when administered in a limited time window after the injury. This presented a need for identifying novel therapeutic targets, preferably early elements of the neuroinflammatory pathway, where inhibition of the immune reaction could have a downstream modulatory effect.

Early components of the inflammasome pathway

The field of inflammasome research emerged in 2002 with the landmark paper of Martinon *et al.* [30], where a molecular complex was first described, which is nowadays known as the inflammasome. Since then, the inflammasome pathway has been identified as an evolutionarily conserved, fundamental component of the innate immune system [31], and a major inducer of pro-inflammatory reactions [32]. As an initial step of immune mechanism activation, elements of the innate immune system rapidly react to the accumulation of damage-associated molecular patterns (DAMPs), which are released to the extracellular space in response to injury. These

include high mobility group box 1 (HMGB1) protein, mitochondrial DNA, amyloid beta, extracellular ATP (eATP), cardiolipin, reactive oxygen species (ROS) and even certain cytokines [33,34]. Sensing of these danger signals by the innate immune system relies on pattern recognition receptors (PRRs), including Nucleotide-binding oligomerization domain-, Leucine-rich Repeat- and Pyrin domain-containing proteins (NLRPs), such as NLRP1, NLRP3 and NLRP6. Activation of these PRRs takes place in two steps: 1) the priming, which includes the increase in the expression of inflammasome components, and 2) an activating step which leads to assembly of inflammasome through oligomerization and recruitment of the adaptor protein Apoptosis-associated Speck-like protein containing a Caspase-recruitment domain (ASC). This in turn binds and induces autoactivation of caspase-1 [30,35]. As a final element of inflammasome activation, pro-inflammatory cytokines interleukin-1β (IL-1β) and IL-18 are processed to their active form and secreted. As a major pro-inflammatory protein, IL-1β is able to further amplify motoneuronal damage through excitotoxicity [36], and regulation of microglia and macrophage recruitment in the nervous system [37]. Furthermore, since IL-1β can also function as a DAMP and can positively regulate NLRP3 priming [38], it can contribute to the over-activation of neuroinflammation.

The NLRP3 inflammasome cascade as a drug target

Initially the NLRP3 inflammasome was identified as a potential drug target in autoimmune diseases, such as systemic lupus erythematosus, rheumatoid arthritis and inflammatory bowel disease [39]. Recently, the involvement of NLRP3 has also been indicated in the pathomechanism of various disorders ranging from type 2 diabetes [40] to neurodegenerative disorders [41], which can be explained by the diversity of inflammasome activators and the complexity of NLRP3 pathway [42]. Based on this, novel small molecule inhibitors were developed in order to target elements of the inflammasome pathway [43], many of which are currently in clinical trials [44]. One of these small molecules is MCC950, a potent inflammasome inhibitor [45], which was shown to attenuate inflammation and improve functional outcome in mouse models of spinal cord injury (SCI) [46], TBI [47] and subarachnoid hemorrhage [48].

Besides directly targeting the NLRP3 inflammasome, earlier elements of the inflammasome pathway also provide potential points of pharmaceutical intervention. Among the wide range of DAMPs that interact with NLRP3, extracellular ATP acts as a multi-target danger signal, which increases neuronal susceptibility to damage, mostly through the P2X purinergic receptor subfamily [49]. The extracellular ATP-mediated P2X4 receptor activation has been

documented to induce activation of the NLRP3 inflammasome in different conditions, such as diabetic nephropathy [50], acute kidney injury [51] and SCI [52]. Furthermore, it has been demonstrated that extracellular ATP-induced NLRP3 activation is linked to the impairment of mitochondrial function [53]. This indicates an intermediary role for mitochondria, where extracellular ATP leads to PRR activation through loss of mitochondrial membrane potential, mitochondrial fragmentation and consequent release of cardiolipin, mitochondrial DNA and ROS [54,55]. This is further supported by experiments where apyrase-induced removal of ATP reduced the mitochondrial damage and IL-1β release in a mouse model of systemic inflammatory response syndrome [56]. Furthermore, activated NLRP3 may translocate to mitochondria-associated endoplasmic reticulum membranes, which provide a platform for NLRP3 inflammasome assembly [57]. These indicate an intricate constellation of interactions between extracellular ATP, NLRP3 inflammasome and mitochondrial dysfunction (Figure 1).

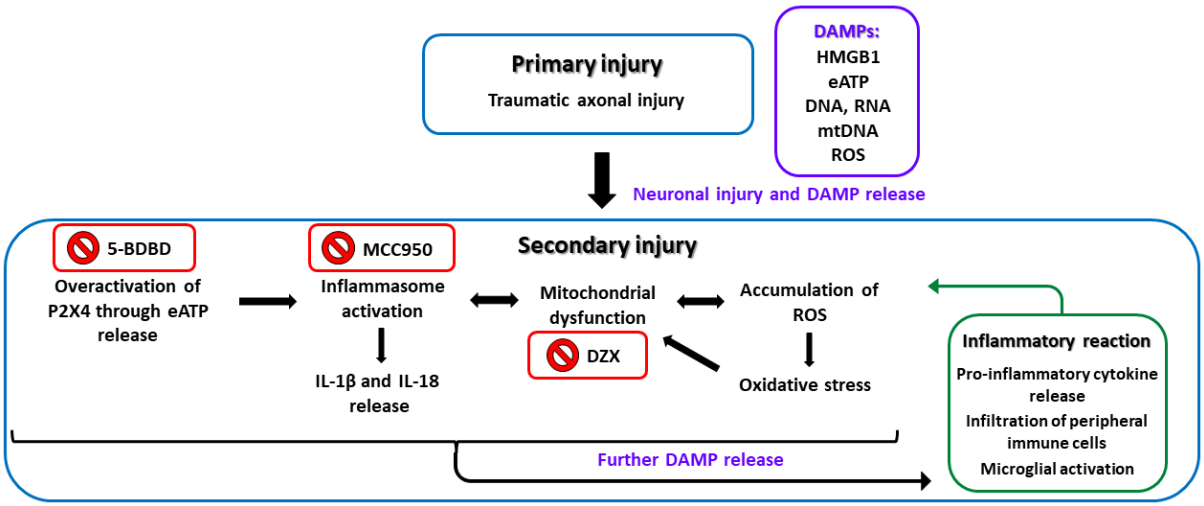

Figure 1. *Schematic summary of the interactions between different mechanisms following peripheral nerve injury. The primary injury results in activation of pro-inflammatory mechanisms, however, secondary mechanisms further fuel these and lead to a self-perpetuating cycle of overactivated inflammatory reaction. Multiple points of therapeutic interventions are also highlighted (red boxes). Note that the interactions presented here do not include all the possible inflammatory pathways, merely a mechanistic representation of inflammasome activation and its interactions with upstream and downstream components. DZX: diazoxide; eATP: extracellular ATP; HMGB1: high mobility group box; IL-1β: interleukin-1β; IL-18: interleukin-18; mtDNA: mitochondrial DNA; ROS: reactive oxygen species.*

Diazoxide (7-chloro-3-methyl-4H-1λ6,2,4-benzothiadiazine 1,1-dioxide, DZX) is a mitochondrial K_{ATP} channel opener, which is considered as a drug with multiple targets

nowadays, which was originally introduced to lower blood pressure and treat hypoglycemia [58]. DZX was documented to exert protective effect on mitochondrial function and structure through restoration of membrane potential in cultured cerebellar granule cells [59] and preserve mitochondrial integrity in pyramidal cells after ischaemia/reperfusion injury [60]. Furthermore, DZX has also been shown to have neuroprotective properties in hypoxic/ischemic injury [61,62]. Recent studies indicated that DZX was able to reduce NLRP3 activation in ischaemia/reperfusion injury by protecting mitochondria [54,63]. Based on this, DZX might act as a potential modulator of the inflammasome pathway, however, its potential anti-inflammatory effect has not yet been analyzed in peripheral nerve injury scenarios.

Aims

In our experiments we aimed at exploring the involvement of the NLRP3 inflammasome pathway in the inflammatory reaction following acute nerve injury and identifying potential therapeutical targets through modulation of the inflammasome response. In our experiments, we used hypoglossal and sciatic nerve transactions and target deprivation of the oculomotor nerve to model peripheral nerve injury in mouse. We primarily investigated the inflammatory changes around the injured motoneuronal cell-bodies in the brainstem and spinal cord, respectively.

Our specific aims were the following:

- to examine and describe the possible activation of the NLRP3 inflammasome after peripheral injury, including the localization and time-dependent changes in the expression of major inflammasome components,
- to evaluate the effect of NLRP3 inflammasome inhibition on other components of the immune response and the regenerative outcome after sciatic nerve injury,
- to assess the involvement of the ATP-P2X4-NLRP3 cascade in the early events following sciatic nerve injury through inhibition of the P2X4 receptor,
- to determine whether the neuroprotective effect of diazoxide (exerted by the modulation of mitochondrial function) is linked to the regulation of the inflammasome cascade and repression of microglial activation.

Methods

Experimental animals, surgical interventions, and pharmacological treatments

8- to 12-week-old male BALB/c mice (mean body weight 23 ± 3 g) were housed and treated in the animal facility of the Biological Research Centre, Szeged. All procedures were approved by the Ethical Committee for the Protection of Animals in Scientific Research at the Biological Research Centre and the Regional Animal Health and Food Control Station of Csongrád-Csanád County (permit number: XVI./767/2018 and XVI./819/2021) and were performed in accordance with widely accepted standards and Hungarian governmental laws related to animal protection.

The number of animals and different experimental groups are summarized in Table 1.

Method	Experiment	Subgroup/treatment	Number of animals used
Immunofluorescence	Colocalization of inflammasome components in the spinal cord, sciatic nerve and DRG following sciatic nerve axotomy	1 day after axotomy	3
		3 days after axotomy	3
		7 days after axotomy	3
	Quantification of NLRP3 and Iba1/GFAP colocalization after sciatic axotomy	7 days after axotomy + vehicle	3
		7 days after axotomy + MCC950	3
	Quantification of axonal regeneration after sciatic axotomy	5 days after axotomy and coaptation + vehicle	3
		5 days after axotomy and coaptation + MCC950	3
Western Blot	Quantification of IL-1β and IL-18 in the hypoglossal nucleus after axotomy	4 days after axotomy	3
Immunohistochemistry	Quantification of NLRP3 in the oculomotor nucleus after axotomy	Intact controls	5
		4 days after axotomy	5
	Quantification of microglial reaction in the hypoglossal nucleus after axotomy	7 days after axotomy	3
		7 days after axotomy + vehicle	3
		7 days after axotomy + DZX	4
	Quantification of NLRP3 in the hypoglossal nucleus after axotomy	Intact controls	5
		4 days after axotomy	5
		4 days after axotomy + vehicle	5
		4 days after axotomy + DZX	5
	Quantification of microglia and astroglia activation in the lumbar spinal cord after sciatic nerve axotomy	3 days after axotomy + vehicle	4
		3 days after axotomy + MCC950	4

		7 days after axotomy + vehicle	4
		7 days after axotomy + MCC950	4
Electron microscopy and brightfield microscopy for cell counting	Quantification of motoneuronal loss and mitochondrial ultrastructure in the hypoglossal nucleus after axotomy	4 days after axotomy	4
		4 days after axotomy + vehicle	4
		4 days after axotomy + DZX	4
		7 days after axotomy	4
		7 days after axotomy + vehicle	4
		7 days after axotomy + DZX	4
Sciatic functional index and retrograde labeling	Quantification of sciatic nerve regeneration after axotomy + coaptation	Axotomy and coaptation	5
		Axotomy and coaptation + vehicle	5
		Axotomy and coaptation + 5-BDBD	5
		Axotomy and coaptation + MCC950	5
Total number of animals			124

Table 1. *Number of experimental animals used in different experimental setups*

Animals underwent either hypoglossal (n = 57), or sciatic nerve (n = 57) axotomy, or unilateral eye enucleation (n = 10). Mice were deeply and reversibly anaesthetized with intraperitoneal injection of Avertin (tribromoethanol, Cat# T48402, Merck-Sigma, St. Louis, MN, USA; 240 mg/kg body weight). In case of hypoglossal axotomy, 1 cm long midline incision was made below the hyoid bone, the right cranial nerve XII. was carefully exposed and a 2-3 mm-long nerve segment was dissected to prevent regeneration. For target deprivation of the oculomotor neurons, the right eyeball was carefully removed, then the orbit was cleared of the remaining extraocular muscles and nerve segments. In case of the sciatic nerve axotomy, the right sciatic nerve was carefully exposed, and a 2-3 mm-long segment was removed at the mid-thigh level. In experimental groups aiming to assay regeneration of sciatic nerve axons, the proximal and distal stumps of the transected nerve were coapted with two epineural sutures (Daclon, Cat# ON105, USP 10/0, EP 0.2, SMI, St. Vith, Belgium), using direct coaptation method under an operating microscope (OM-5, Takagi Seico, Tokyo, Japan) immediately after transection. The wound was closed with Vetbond™ tissue adhesive (Cat# 1469SB, 3 M, St. Paul, MN, USA).

Operated animals received intraperitoneal injection of 10 mg/kg body weight MCC950 (Cat# inh-mcc, Invivogen, San Diego, CA, USA) 1 hour after axotomy or 5 mg/kg body weight 5-BDBD (Cat# 3579, Tocris Bioscience, Bristol, UK) 30 min after injury and then every 24 h up to the third postoperative day. In the DZX-treated experimental groups, animals received DZX (Cat# D9035, Merck-Sigma) treatment in the form of intraperitoneal injections of 1 mg/kg

body weight, 1 hour after axotomy, then once every 24 hours for 3 days. Vehicle group received equal amount of dimethyl-sulfoxide (DMSO) (Cat# D2650, Merck-Sigma) in phosphate buffered saline (PBS) intraperitoneally.

Immunohistochemistry (IHC) and immunofluorescent (IF) staining and imaging

Axotomized animals were perfused with 10 mM PBS (pH = 7.4), followed by fixation with 4 % paraformaldehyde (PFA) in 10 mM PBS. The brainstem, spinal cord, the dorsal root ganglion (DRG) and the injured sciatic nerve segments were exposed and removed, then fixed further overnight in the same fixative at 4 °C. Next day the fixative was removed, and the tissue was directly placed in 30 % sucrose (Cat# 02200-203-190, Molar Chemicals, Halásztelek, Hungary) dissolved in 10 mM PBS, at least for 1 day at 4 °C. Spinal cord and brainstem samples were mounted onto a freezing microtome (Reichert-Jung, Leica Biosystems, Wetzlar, Germany) and 30 µm-thick sections were cut from the L4–L5 lumbar segment or the anatomical region of the oculomotor or hypoglossal nucleus. Sections were kept in 10 mM PBS with 0.05 % sodium azide (Cat# S2002, Merck-Sigma) until further processing. DRG and sciatic nerve samples were cut with a Leica CM1860 cryostat, and 10 µm-thick sections were mounted and frozen onto silane-coated glass slides (Cat# 631-1163, VWR International, Radnor, PA, USA). These sections were kept at -20 °C until use.

IHC stainings were performed on 30 µm-thick free-floating brainstem or spinal cord sections. For the quantitative evaluation of changes in NLRP3, ionized calcium-binding adaptor molecule 1 (Iba1) and glial fibrillary acidic protein (GFAP) expression, diaminobenzidine tetrahydrochloride (DAB)-based visualization protocol was performed. Sections were rinsed in 10 mM PBS three times, then to block the endogenous peroxidase activity, the tissue was incubated in 0.6 % hydrogen peroxide in 10 mM PBS containing 0.2 % Triton X-100 (Cat# T9284, Merck-Sigma) (TPBS) for 30 min. After washing steps with 10 mM PBS, 2 % normal goat serum (Cat# S-1000, RRID:AB_2336615, Vector Laboratories, Burlingame, CA, USA) in TPBS was applied for 60 min to block nonspecific binding sites. Primary antibodies (Table 2) were diluted in blocking solution and sections were incubated overnight at 4 °C on an orbital shaker (50-60 rpm). Sections were then extensively washed in 10 mM PBS. This was followed by incubation at room temperature with biotinylated secondary antibody (Table 2) diluted in blocking solution for 60 min. Sections were rinsed in 10 mM PBS three times, incubated in avidin-biotin complex (Cat# PK-6100, RRID:AB_2336819, Vector Laboratories) diluted to 1:800 in PBS for 60 min at room temperature. After thoroughly washing in 10 mM PBS, reactions were visualized by incubation in 0.05 % DAB (Cat# 34001, Thermo Fisher Scientific)

with 1.5 % NiCl2 in 10 mM PBS for 15 min. Finally, sections were washed in 10 mM PBS, rinsed in tri-distilled water, mounted with Entellan (Cat# 107961, Merck Millipore, Darmstadt, Germany) and visualized under a brightfield microscope (Eclipse 80i, RRID:SCR_015572, Nikon, Tokyo, Japan).

IF staining protocols were also performed on 30 µm-thick free-floating lumbar spinal cord and brainstem sections and the previously mounted DRG and sciatic nerve sections. First, sections were rinsed as previously described. Afterward, blocking step was used with 2 % normal donkey serum (Cat# 017–000-121, RRID:AB_2337258, Jackson ImmunoResearch) in 10 mM TPBS for 60 min. Primary antibody cocktails (Table 2) in blocking solution were applied for overnight incubation at 4 °C. The next day, sections were rinsed, and secondary antibody cocktails (Table 2) were used for 60 min. Finally, sections were washed in 10 mM PBS three times and, where indicated, Hoechst 33342 (Cat# B2261, Merck-Sigma) staining was applied (diluted to 1 µg/ml in 10 mM PBS) to visualize cell nuclei. Sections were mounted on silane-coated glass slides (if not mounted previously), covered with Fluoromount-G (Cat# 0100–01, Southern Biotech, Birmingham, AL, USA) mounting medium. Secondary antibody staining controls have been carried out for each of the applied secondary antibodies to exclude the interference of any associated unspecific staining.

Stainings	**Primary antibodies**	**Secondary antibodies**
IL-1β (WB)	polyclonal goat against IL-1β, 1:500 (Cat# AF-401-NA, RRID:AB_416684, R&D Systems)	HRP-conjugated Rabbit anti-Goat IgG (H+L), 1:4000 (Cat# A5420, RRID:AB_258242, Merck-Sigma)
IL-18 (WB)	polyclonal rabbit against IL-18, 1:500 (Cat# 5180R-100, RRID:AB_2123793, BioVision Incorporated)	HRP-conjugated Goat anti-Rabbit IgG (H+L), 1:4000 (Cat# 111-035-003, RRID:AB_2313567, Jackson ImmunoResearch)
β-actin (WB)	monoclonal mouse against β-actin, 1:10000 (Cat# A5441, RRID:AB_476744, Merck-Sigma)	HRP-conjugated Goat anti-Mouse IgG (H+L), 1:4000 (Cat# 115-035-003, RRID:AB_10015289, Jackson ImmunoResearch)
Iba1 (IHC)	polyclonal rabbit against Iba1, 1:500 (Cat# 019-19741, RRID:AB_839504, FUJIFILM Wako Pure Chemical Corporation, Osaka, Japan)	Biotinylated Goat anti-Rabbit IgG Antibody (H+L), 1:500 (Cat# BA-1000, RRID:AB_2313606, Vector Laboratories)
GFAP (IHC)	polyclonal rabbit against GFAP, 1:500 (Cat# ab16997, RRID:AB_443592, Abcam, Cambridge, UK)	Biotinylated Goat anti-Rabbit IgG Antibody (H+L), 1:500 (Cat# BA-1000, RRID:AB_2313606, Vector Laboratories)
ASC (IHC)	monoclonal mouse against ASC, 1:400 (Cat# sc-271054, RRID:AB_10608960, Santa Cruz Biotechnology, Dallas, TX, USA)	Biotinylated Goat anti-Mouse IgG Antibody (H+L), 1:800 (Cat# BA-9200, RRID:AB_2336171, Vector Laboratories)
NLRP3 (IHC)	polyclonal goat against NLRP3, 1:500 (Cat# GTX88190, RRID:AB_10723786 GeneTex, Irvine, CA, USA)	Biotinylated Rabbi anti-Goat IgG Antibody (H+L), 1:800 (Cat# BA-5000, RRID:AB_2336126, Vector Laboratories)
NLRP3 (IF)	polyclonal goat against NLRP3, 1:100 (Cat# GTX88190, RRID:AB_10723786 GeneTex, Irvine, CA, USA)	Alexa Fluor® 594 Plus Highly Cross-Adsorbed Donkey anti-Goat IgG (H+L),

		1:500 (Cat# A32758, RRID:AB_2762828, Thermo Fisher Scientific)
AQP4 (IF)	polyclonal rabbit against AQP4, 1:100 (Cat# sc-390488, Santa Cruz Biotechnology)	Alexa Fluor® 488 AffiniPure Donkey anti-Rabbit IgG (H+L), 1:500 (Cat# 711-545-152, RRID:AB_2313584, Jackson ImmunoResearch)
ASC (IF)	monoclonal mouse against ASC, 1:100 (Cat# sc-271054, RRID:AB_10608960, Santa Cruz Biotechnology, Dallas, TX, USA)	Alexa Fluor® 647 Plus Highly Cross-Adsorbed Donkey anti-Mouse IgG (H+L), 1:500 (Cat# A32787, RRID:AB_2762830, Thermo Fisher Scientific)
	monoclonal rabbit against ASC, 1:100 (Cat# 67824, RRID:AB_2799736, Cell Signaling Technology, Danvers, MA, USA)	Alexa Fluor® 488 AffiniPure Donkey anti-Rabbit IgG (H+L), 1:500 (Cat# 711-545-152, RRID:AB_2313584, Jackson ImmunoResearch)
NeuN (IF)	polyclonal rabbit against NeuN, 1:4000 (Cat# ABN78, RRID:AB_10807945, Merck Millipore)	Alexa Fluor® 488 AffiniPure Donkey anti-Rabbit IgG (H+L), 1:500 (Cat# 711-545-152, RRID:AB_2313584, Jackson ImmunoResearch)
ChAT (IF)	polyclonal rabbit against ChAT, 1:250 (Cat# GTX113164, RRID:AB_1949973, GeneTex)	Alexa Fluor® 488 AffiniPure Donkey anti-Rabbit IgG (H+L), 1:500 (Cat# 711-545-152, RRID:AB_2313584, Jackson ImmunoResearch)
	polyclonal goat against ChAT, 1:500 (Cat# AB144, RRID:AB_90650, Merck Millipore)	Alexa Fluor® 488 Cross-Absorbed Donkey anti-Goat IgG (H+L), 1:500 (Cat# A11055, RRID:AB_2534102, Thermo Fisher Scientific)
GFAP (IF)	polyclonal rabbit against GFAP, 1:500 (Cat# ab16997, RRID:AB_443592, Abcam)	Alexa Fluor® 488 AffiniPure Donkey anti-Rabbit IgG (H+L), 1:500 (Cat# 711-545-152, RRID:AB_2313584, Jackson ImmunoResearch)
		Alexa Fluor® 647 AffiniPure Donkey anti-Rabbit IgG (H+L), 1:500 (Cat# 711-605-152, RRID:AB_2492288, Jackson ImmunoResearch)
Iba1 (IF)	polyclonal rabbit against Iba1, 1:500 (Cat# 019-19741, RRID:AB_839504, FUJIFILM Wako Pure Chemical Corporation)	Alexa Fluor® 488 AffiniPure Donkey anti-Rabbit IgG (H+L), 1:500 (Cat# 711-545-152, RRID:AB_2313584, Jackson ImmunoResearch)
TRPV1 (IF)	polyclonal rabbit against TRPV1, 1:500 (Cat# ACC-030, RRID:AB_2313819, Alomone Labs, Jerusalem, Israel)	Alexa Fluor® 488 AffiniPure Donkey anti-Rabbit IgG (H+L), 1:500 (Cat# 711-545-152, RRID:AB_2313584, Jackson ImmunoResearch)
p75 (IF)	monoclonal mouse against p75 NGF receptor, 1:500 (Cat# ab6172, RRID:AB_305340, Abcam)	Alexa Fluor® 647 Plus Highly Cross-Adsorbed Donkey anti-Mouse IgG (H+L), 1:500 (Cat# A32787, RRID:AB_2762830, Thermo Fisher Scientific)
NEFM (IF)	monoclonal recombinant rabbit against NEFM, 1:500 (Cat# MA5-32613, RRID:AB_2809890, Thermo Fisher Scientific)	Alexa Fluor® 488 AffiniPure Donkey anti-Rabbit IgG (H+L), 1:500 (Cat# 711-545-152, RRID:AB_2313584, Jackson ImmunoResearch)

Table 2. *List of primary and secondary antibodies used for western blot (WB), immunohistochemistry (IHC) and immunofluorescence (IF). IL-1β: interleukin-1β; IL-18: interleukin-18; Iba1: ionized calcium-binding adaptor molecule 1; GFAP: glial fibrillary acidic protein; ASC: Apoptosis-associated Speck-like protein containing a Caspase-recruitment domain; NLRP3: Nucleotide-binding oligomerization domain-, Leucine-rich*

Repeat- and Pyrin domain-containing protein 3; AQP4: aquaporin-4; NeuN: neuronal nuclei protein; ChAT: choline acetyltransferase; TRPV1: transient receptor potential vanilloid 1; p75: p75 neurotrophin receptor, also known as low-affinity nerve growth factor receptor; NEFM: neurofilament medium polypeptide.

Confocal images were obtained with a Leica TCS SP5 laser scanning microscope (RRID:SCR_020233, Leica Biosystems). Images were taken with a HCX PL APO CS 20 × /0.7 or HCX PL APO lambda blue 63 × /1.4 oil objective in 1024 × 1024 resolution. Multiple images were taken from approx. 20 µm depth of field (at distances of 1 µm) and merged into z-projections in Las X Viewer (RRID:SCR_013673, Leica Biosystems) or in FIJI (Fiji is just ImageJ, RRID:SCR_002285, Max Planck Institute of Molecular Cell Biology and Genetics, Dresden, Germany) software. Super-resolution images were obtained with a STEDYCON (Abberior Instruments) stimulated emission depletion (STED) microscopy instrument connected to a ZEISS Axio Observer Z1 inverted microscope. In the result section of the thesis, z-stacks are presented, and in some cases, pseudocolors are used to simplify the visualization of certain stainings. Brightness and contrast were adjusted as needed.

Quantification of the NLRP3, microglia and astroglia staining

The quantification method was previously developed in our laboratory, based on an interactive macro for the Image-Pro Plus image analysis software (RRID:SCR_016879, Media Cybernetics, Rockville, MD, USA). Briefly, brain stem or spinal cord sections were stained for microglia (Iba1), NLRP3 or astroglia (GFAP), then both the control and injured motor nuclei/ventral horns on the sections were captured with a Nikon Eclipse 80i microscope equipped with a 2560 × 1920 pixel resolution MicroPublisher 5.0 RTV charge-coupled device camera at 20 × magnification. During the image analysis, a consistent background subtraction algorithm was applied, based on internal controls (intact side) in each section, to determine the significantly stained profiles in identical regions at both the operated and contralateral sides of the spinal cord and brainstem nuclei. This resulted in an automated, unbiased evaluation protocol as the algorithm determined the stained profile values with the same background subtraction for both the injured and contralateral sides on each section. Lastly, we averaged the algebraic differences between the operated and control sides. Microglial, astroglial and NLRP3 stainings were all evaluated with this method.

In order to quantify the ratio of neurons in which the translocation of NLRP3 from the cell nuclei to the cytoplasm could be observed, a cell-counting procedure was carried out. From the

non-treated axotomized group (hypoglossal axotomy), sections were selected from the hypoglossal nucleus of each animal (n = 5 animals). Neuronal cells were identified based on their size and the anatomical boundaries. On each of the sections, NLRP3 positive neurons were counted based on the localization of the staining. If NLRP3 was only present in the neuronal nucleus, the expression was counted as "nuclear NLRP3". If NLRP3 staining was clearly present in the cytoplasm, the expression was counted as "cytoplasmic NLRP3". When NLRP3 was clearly present in both the cytoplasm and nucleus, cells were sorted in the "cytoplasmic NLRP3" group, since the nuclear NLRP3 expression was recognized as the basal expression and the cytoplasmic presence of NLRP3 indicated translocation. Neurons were only counted if a well-described point of reference (cell nucleus) could be recognized in the section. Neurons were counted on both the operated and the control side. The ratio of translocation was determined for each side of each section and was averaged.

Morphological analysis of microglial cells after hypoglossal axotomy

Microglial morphology was quantified according to the work of Fernández-Arjona *et al.* [64]. Sections were screened under Nikon Eclipse 80i light microscope on 40× magnification. 10-10 microglial cells were captured with extended depth of field imaging from both the control and injured sides of the hypoglossal nucleus to visualize the complete arborization of the microglial processes. Images were then processed with Photoshop (Adobe, San Jose, CA, USA) to extract single microglial cells. Contrast and brightness were adjusted to achieve the best cell structure visibility. Images were then converted to binary images in ImageJ and further corrected in Photoshop. From the segmented microglia, area and perimeter of the cell were extracted by ImageJ and the following parameters were measured with the help of Box Counting Fractal Analysis method using FracLac plugin in ImageJ: cell area, cell perimeter, fractal dimension, lacunarity, convex hull (CH) span ratio, CH area, CH perimeter, CH circularity, max/min radii, mean radius and diameter of bounding circle [65]. Density, cell circularity, and roughness were then calculated. All data were normalized in order to serve as an input to clustering algorithms, then processed with Weka Explorer [66], an open-source data mining software package. Data was automatically divided into two different clusters with the k-means-based Farthest-First clustering algorithm [67].

Quantification of motoneuronal survival after hypoglossal axotomy

Motor neurons were counted under Eclipse 80i (Nikon, Tokyo, Japan) light microscope in a set of equidistantly (at 60 μm) placed sections, selected from the collection of consecutively cut sections from the hypoglossal nucleus of each animal. The motor neurons were identified by

their size, their anatomical localization and their morphological features. To satisfy the selection criterion of the dissector method, *i.e.*, to identify the object to be counted with its single, point-like structure, motor neurons with discernible nuclei were counted. From each animal (n = 4/group), 10–10 sections were screened for the presence of motor neurons. Finally, the ratio of motoneurons was determined compared to the control (intact side).

Tissue preparation for electron microscopy and analysis of mitochondrial morphometry

For electron microscopic evaluation animals were transcardially perfused with 10 mM PBS then fixed in Karnovsky solution [68]. Hypoglossal nuclei were removed and fixed in the same fixative for 4 h at room temperature, rinsed and postfixed in 2 % osmium tetroxide solution. After dehydration with an ascending series of ethanol, the samples were embedded in epoxy resin (Durcupan ACM, Sigma, USA) and polymerized at 56 °C for 2 days. Ultrathin sections (50 nm) were then prepared and contrasted with uranyl acetate and lead citrate. Alterations of the mitochondria are routinely detected with morphometric parameters such as perimeter, area or Feret's diameter, *i.e.*, the longest distance between any two points of the mitochondrial external perimeter [69,70]. Since increased Feret's diameter could be observed in oxidative stress [71,72], we selected this parameter to evaluate whether reduced oxidative stress could be achieved by DZX treatment. Transmission electron microscope (JEM-1400Flash; JEOL, Tokyo, Japan) was used in conventional transmission mode (120 kV) to capture mitochondria of motor neurons and microglial cells, using a scientific complementary metal–oxide semiconductor camera (Matataki Flash; JEOL) at 12 000× magnification. 10-10 images were captured from different motor neurons and microglia from both sides. Images obtained with electron microscope were used for examining the changes in mitochondrial morphology. Each mitochondrion from all images was segmented and morphometric parameters were measured with the built-in functions of Image-Pro Plus.

Tissue preparation and western blot

Under irreversible anesthesia with Avertin, mice were transcardially perfused with 10 mM PBS. The entire brain was exposed, removed and placed in 10 mM PBS, then dissected in the following manner: first, the brain was coronally sliced at approximately -6 mm from Bregma (at the medulla oblongata – pons transition), then at -7.5 mm from Bregma (at the appearance of the *decussatio pyramidum*). Next, the cerebellum was carefully removed from the sample. From the remaining sample, 1 mm-wide lateral segments were sliced and removed along the sagittal plane on both sides. From the ventral part of the medulla oblongata, a 0.5 mm wide segment was cut and removed horizontally. Finally, the sample was sliced along the mid-

sagittal axis and the two sides (injured and control sides) were separated and placed into sample holders.

Snap-freezing in liquid nitrogen was performed immediately after tissue dissection, then samples were processed in a Potter-Elvehjem homogenizer with a polytetrafluoroethylene pestle in 10 mM PBS. Samples were ground on ice until they were completely homogeneous. Samples were centrifuged twice at 6000 × g for 8 min at 4 °C to remove debris. An equal volume of methanol and 1/4 volume of chloroform were added. Samples were vortexed, incubated for 5 min on ice, and centrifuged at 13000 × g for 5 min at 4 °C. After phase separation, the aqueous phase was removed, and protein samples were washed with ice-cold methanol. Samples were vortexed and centrifuged again, supernatants were discarded, and protein pellets were air-dried. Pellets were then reconstituted in 2× Laemmli buffer and heated up to 95 °C for 5 min. Protein concentration was determined by using bicinchoninic acid assay (BCA, Cat# 23225, Thermo Fisher Scientific).

Samples were electrophoresed using standard denaturing SDS/PAGE and blotted onto polyvinylidene difluoride membranes (PVDF; 0.2 μm pore size; Cat# 162–0177, Bio-Rad). After blocking with 3 % bovine serum albumin (BSA; Cat# 97061-422, VWR International) in Tris-buffered saline with 0.1 % Tween-20 (TBS-T), membranes were incubated with primary antibodies (Table 2) overnight at 4 °C. Blots were washed in TBS-T three times for 10 min, incubated for 1 h in horseradish peroxidase-conjugated secondary antibodies (Table 2) diluted in TBS-T, and then washed again in TBS-T. Immunoreaction was visualized with Clarity Chemiluminescence Substrate (Cat# 1705061, Bio-Rad) in a ChemiDoc MP System (RRID:SCR_019037, Bio-Rad). Densitometry analysis was performed with the Image lab software, version 5.2 (RRID:SCR_014210, Bio-Rad).

Sciatic functional index (SFI) measurements

The SFI is a well-characterized index, widely used to study peripheral nerve regeneration in both sciatic nerve cursh and nerve axotomy models. To assess the regeneration of the sciatic nerve following injury, SFI measurements were carried out 1 day before the axotomy + nerve coaptation and on post-operative days 3, 7 and then on every seventh day up to 8 weeks. The measurements were carried out on untreated, vehicle-treated (DMSO), 5-BDBD-treated and MCC950-treated animals. Treatments were administered as described earlier. A non-toxic dye was used to register the hind paw print of the animals during the walking track analysis. Since earlier studies found that paw length and toe spread are the significant indicators of sciatic

function in mouse, we used these parameters and the reworked SFI formula for mouse: SFI=118.9∗(ETS-NTS)/NTS-(51.2∗(EPL-NPL)/NPL))-7.5, where NTS: normal toe spread, NPL: normal paw length, ETS: experimental toe spread, EPL: experimental paw length [73]. At the endpoint of the experiments, the same animals were used for Fast blue (FB) tracer analysis.

Retrograde labeling experiments after sciatic axotomy

Eight weeks after the surgery, animals were anaesthetized as described above. On the operated side, the sciatic nerve was cut 2 mm distally to the zone of coaptation and the proximal stump of the nerve was covered with FB crystals (Cat# 17740-5, Polysciences Europe GmbH, Hirschberg an der Bergstrasse, Germany) [74]. On the intact side, the same surgical procedure was performed. Four days after the application of this fluorescent dye, the animals were re-anaesthetized and were transcardially perfused with 4 % PFA in 10 mM PBS. Sample preparation was carried out as described earlier for IF staining.

After sectioning of the spinal cord samples, the following routine was applied for the selection of sections for staining: one section (30 μm-thick) was collected, then the next two consecutive sections were omitted (altogether 60 μm-thick). Then, choline acetyltransferase (ChAT) IF staining was used to label motoneurons. During the cell counting procedure, the ventral horns of both the control and injured sides were captured (on Nikon Eclipse 80i microscope) on each selected section. FB-positive cells were only counted if they were ChAT-positive as well, and the cell nucleus was clearly visible. Thus, it was ensured that each motoneuron was only counted once. The number of FB-positive motoneurons was then summed on each side and a ratio was calculated (injured/intact side).

Statistical analysis

All statistical analyses were performed with GraphPad Prism (version 8.0.1.244, RRID:SCR_002798, GraphPad Software, San Diego, CA, USA). The type of statistical analysis is indicated in each figure legend. Data is presented as mean ± standard error of the mean (SEM). In order to determine the number of animals needed, power analysis was carried out with G* Power (RRID:SCR_013726) [75]. All experiments were performed in a blinded manner.

Results

NLRP3 expression in the hypoglossal and oculomotor nucleus following axotomy

In our first experiment, changes in the NLRP3 expression were assessed in the oculomotor and hypoglossal nucleus 4 days after hypoglossal nerve axotomy or oculomotor target deprivation injury. Under control (*i.e.*, intact) conditions, a faint basal NLRP3 staining was present in both sides of the oculomotor and hypoglossal nuclei in mouse brain sections. Target deprivation in the case of the oculomotor nucleus led to the increase in the area of the NLRP3 staining which was absent on the contralateral side serving as an internal control (Figure 2A). Similar change was visible in the hypoglossal nucleus after hypoglossal axotomy; however, the reaction was more intense (Figure 2A).

The staining morphology suggested that the majority of NLRP3-positive cells were neurons. Therefore, double stainings with neuronal nuclei protein (NeuN) and ChAT markers were performed (Figure 2B). Since a more intense reaction was observed in the hypoglossal nucleus compared to the oculomotor nucleus, experiments in the hypoglossal axotomy model were resumed. NeuN staining decreased in the affected motor nucleus compared to the contralateral side, reflecting a neuronal response to axotomy, as described by others [76,77]. As anticipated, the majority of NLRP3-positive cells were NeuN-positive (Figure 2B), indicating neuronal NLRP3 upregulation. ChAT staining almost completely overlapped with NLRP3 staining, indicating that indeed motoneurons expressed NLRP3 (Figure 2B). However, at the side of the lesion, ChAT staining, similarly to NeuN staining, decreased due to the disturbance in the neuronal homeostasis [78].

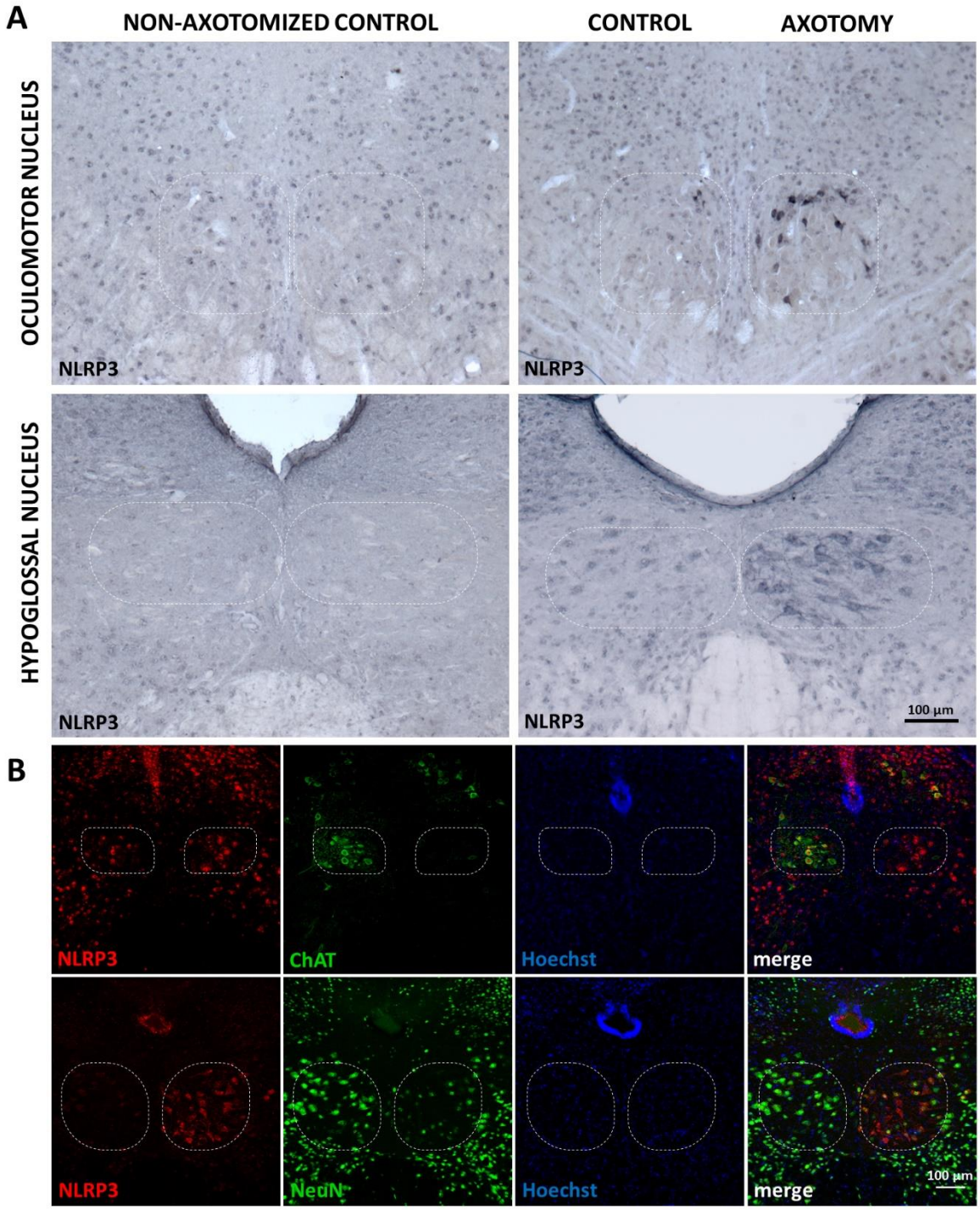

Figure 2. *NLRP3 protein expression in motor neurons of the oculomotor and hypoglossal nuclei 4 days after hypoglossal nerve axotomy or oculomotor target deprivation. (A) Representative immunohistochemical stainings of NLRP3 protein on mouse brainstem sections from the oculomotor (top panel) and hypoglossal (bottom panel) nuclei following axotomy. (B) Representative fluorescence immunostaining images of NLRP3, ChAT (top panel) and NeuN (bottom panel) proteins in the hypoglossal nucleus after brain nerve axotomy. Nuclei were counterstained with Hoechst 33342. Scale bar: 100 µm.*

In order to identify further cell types that might respond with the upregulation of NLRP3 to peripheral nerve injury, double staining with Iba1 (a microglial marker) (Figure 3A) and GFAP (an astroglial marker) (Figure 3B) was performed. Interestingly, 4 days after the axotomy, the majority of the microglia were not stained with the NLRP3 antibody, only a few microglial cells were NLRP3-positive. Similarly, NLRP3 was upregulated only in a small fraction of astrocytes, and astrocytic endfeet were largely excluded as demonstrated by the double staining with the astrocyte endfeet marker aquaporin-4 (AQP4) (Figure 3C).

Quantitative analysis revealed that the NLRP3 increase was significant in both the oculomotor nucleus (8.04 ± 1.98 vs. 2.66 ± 0.34 %; injured vs. intact; $p < 0.05$) and the hypoglossal nucleus (27.25 ± 4.87 vs.1.13 ± 0.51 %; $p < 0.001$) after the nerve transection, when compared to the contralateral (intact) side. Furthermore, NLRP3 increase was significantly lower in the oculomotor nucleus compared to the hypoglossal nucleus following axotomy (8.04 ± 1.98 vs. 27.25 ± 4.87 %; injured oculomotor nucleus vs. injured hypoglossal nucleus; $p < 0.001$).

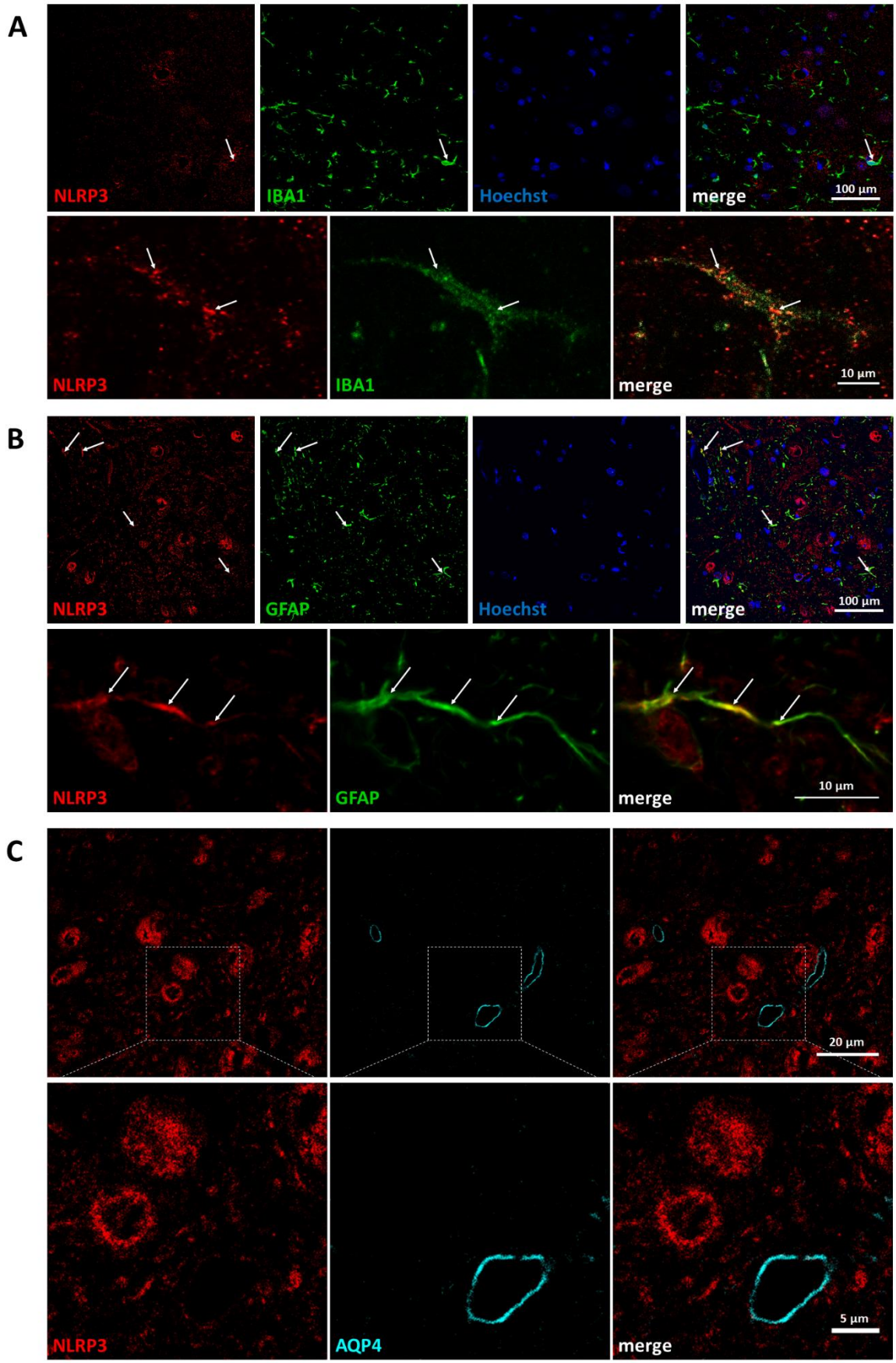

Figure 3. *Partial colocalization of NLRP3 with glial marker proteins but not with microvessels*

on the injured side 4 days after hypoglossal nerve axotomy. (A) Representative STED images of NLRP3 and Iba1 immunofluorescent in the hypoglossal nucleus following hypoglossal nerve axotomy. Top panels: lower magnification (Scale bar: 100 µm); bottom panels: high magnification (Scale bar: 10 µm). (B) Representative confocal STED images of NLRP3 and GFAP immunofluorescent stainings from the anatomical region of the hypoglossal nucleus after axotomy. Top panels: lower magnification (Scale bar: 100 µm); bottom panels: high magnification (Scale bar: 10 µm). (C) Representative confocal STED images of NLRP3 and astroglial endplates (AQP4) stainings in the hypoglossal nucleus following axotomy. Top panels: lower magnification (Scale bar: 20 µm); bottom panels: high magnification (Scale bar: 5 µm). Arrows indicate colocalization of the stainings. Nuclei were counterstained with Hoechst 33342.

Subcellular distribution of NLRP3 and inflammasome activation following hypoglossal axotomy

In intact hypoglossal nucleus and on the intact side of the hypoglossal nucleus after axotomy the majority of NLRP3 staining was located in the nuclei of neurons. In response to the transection of the hypoglossal nerve, the staining appeared mainly in the cytoplasm, in parallel to the weakening of the nuclear NLRP3 staining (Figure 4A), indicating nucleo-cytoplasmic translocation. In order to visualize these changes more accurately and to carry out quantitative analysis, IHC stainings were performed which confirmed the observations obtained with fluorescence staining (Figure 4B). Quantitative analysis revealed that the ratio of neurons showing cytoplasmic NLRP3 was significantly higher on the injured side of the hypoglossal nucleus following axotomy (82.24 ± 5.38 vs. 1.95 ± 1.33 %; injured side vs. intact side; $p < 0.001$) (Figure 4C).

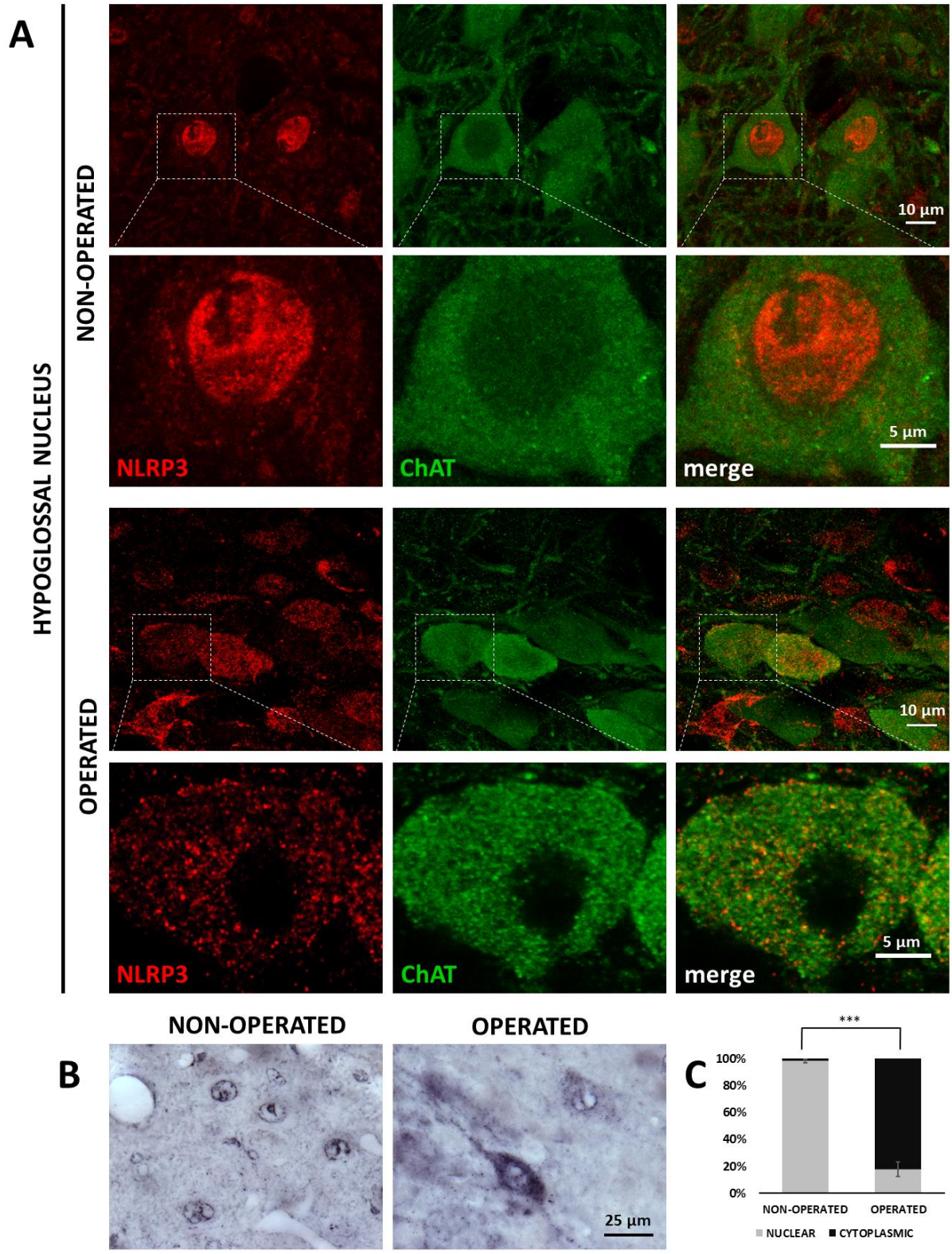

Figure 4. *NLRP3 translocation from neuronal cell nuclei to the cytoplasm in response to hypoglossal nerve axotomy. (A) Representative super-resolution microscopy images of NLRP3 and motoneuronal (ChAT) staining of mouse hypoglossal nucleus from the non-operated (intact) and operated side after hypoglossal nerve axotomy. Top panels (on both the non-*

*operated and operated sides): lower magnification (scale: 10 μm); bottom panels: high magnification (Scale bar: 5 μm). (B) Representative immunohistochemical staining images of NLRP3 staining in the hypoglossal nucleus, from the non-operated (left panel) and operated (right panel) sides after nerve axotomy (Scale bar: 25 μm). (C) Quantification of subcellular distribution of NRLP3 staining in neurons from non-operated and operated sides of the hypoglossal nucleus. The graph shows average % ± SEM of neurons in which NLRP3 localized in the nucleus or the cytoplasm (n = 5 animals/group, *** = p < 0.001) (Student's paired t-test).*

The activation of inflammasomes involves formation of a multiprotein complex, which includes the binding of NLRP3 with the adaptor molecule ASC. Therefore, colocalization analysis was performed. Similarly to NLRP3, ASC was also upregulated after nerve transection in the hypoglossal nucleus (Figure 5A). Immunofluorescent staining performed with NLRP3, and ASC showed significant overlap of the stainings, mainly in neurons (Figure 5B). Interestingly, the colocalization could be observed in the neuronal nuclei as well (Figure 5C). Although NLRP3 could be detected in GFAP-positive cells as well, there was almost no colocalization with ASC (Figure 5C), indicating a neuron-specific inflammasome formation following axotomy. Colocalization of NLRP3 and ASC in microglial cells could not be detected either (data not shown).

To further examine NLRP3 inflammasome activation, the protein levels of active IL-1β and IL-18, the main pro-inflammatory cytokines of the inflammasome pathway, were quantified with western blot. These changes were also evaluated in the hypoglossal nucleus following axotomy of the hypoglossal nerve, since more intense NLRP3 upregulation was observed here compared to the oculomotor nucleus. Axotomy resulted in a 1.507-fold increase of pro-IL-1β levels ($p < 0.001$), indicative of the priming stage of inflammasome activation. In addition, a 1.873-fold increase of the active IL-1β levels was detected in the axotomized hypoglossal nucleus compared to the control side ($p < 0.05$) (Figures 5D,E). Similarly, a 1.893-fold increase was observed in the active IL-18 levels after axotomy ($p < 0.05$) (Figures 5D,F).

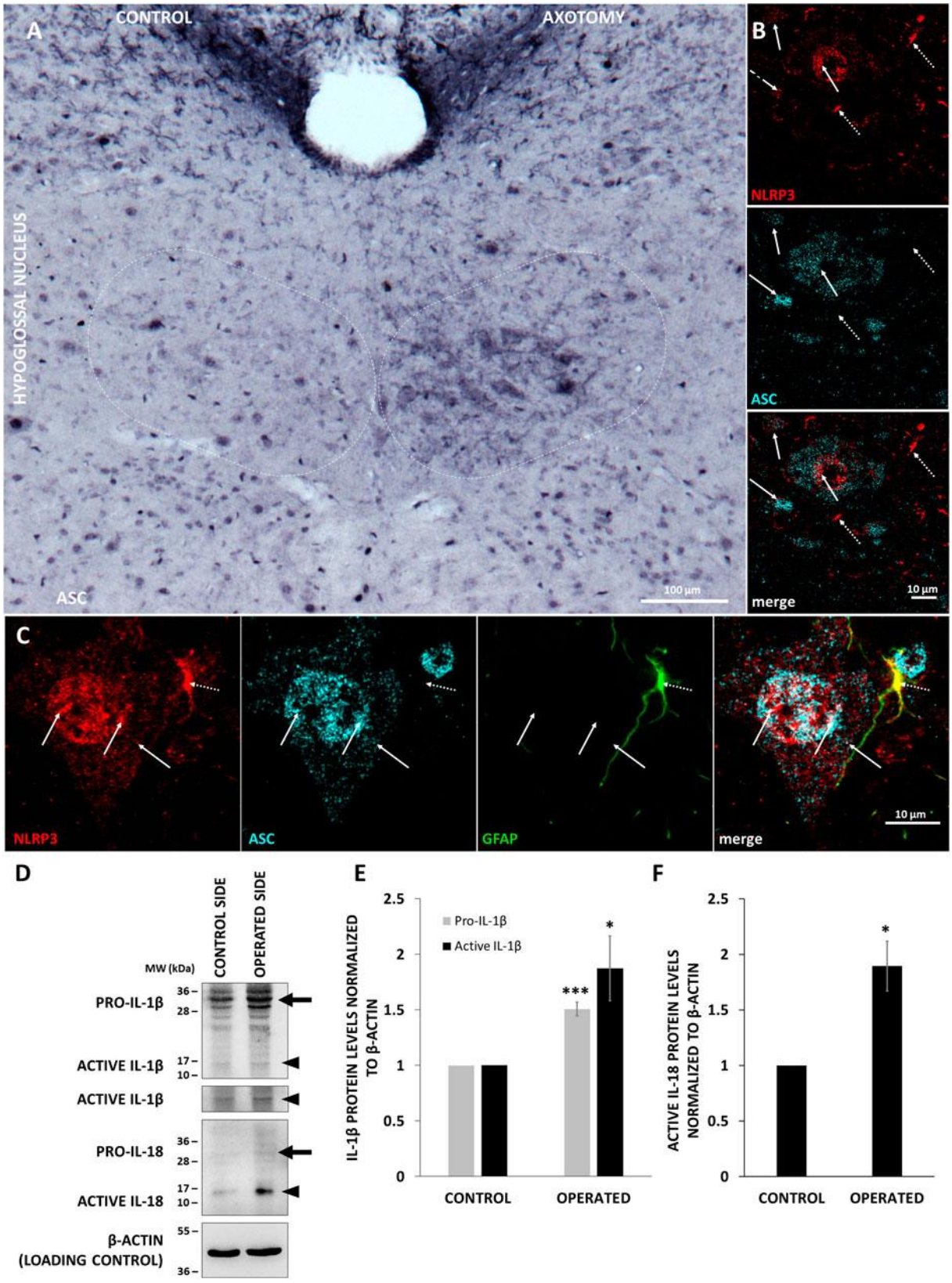

Figure 5. *Colocalization of inflammasome components and upregulation and activation of IL-1β and IL-18 in the hypoglossal nucleus. (A) Representative images of ASC staining in the hypoglossal nucleus after axotomy (Scale bar: 100 µm). (B) Representative STED images of*

*NLRP3 and ASC staining in the hypoglossal nucleus following axotomy (Scale bar: 10 μm). Solid arrows indicate the colocalization of NLRP3 and ASC. Dashed arrows indicate NLRP3 without colocalization with ASC. (C) Representative STED images of NLRP3, ASC and GFAP staining in the hypoglossal nucleus after axotomy (Scale bar: 10 μm). Solid arrows indicate colocalization of NLRP3 and ASC in the nucleus and cytoplasm of the cells. Dashed arrow indicates colocalization of NLRP3 with GFAP, but not with ASC. (D) Representative western blot images of IL-1β and IL-18 proteins in the hypoglossal nucleus after hypoglossal axotomy. Arrows indicate pro-forms, arrowheads show active cytokines. (E) Quantification of pro- and active IL-1β expression is based on the western blot analysis of the hypoglossal nuclei in n = 3 animals. The graph shows values normalized to β-actin levels and to control side (average ± SEM, * = p < 0.05; *** = p < 0.001) (Student's paired t-test). (F) Quantification of active IL-18 expression based on the western blot analysis of the hypoglossal nucleus in n = 3 animals. The graph shows values normalized to β-actin levels and to control side (average ± SEM, * = p < 0.05) (Student's paired t-test).*

Effect of diazoxide on NLRP3 expression after hypoglossal nerve axotomy

Next, we aimed to investigate the effect of the neuroprotective agent DZX on the axotomy-induced NLRP3 upregulation, thus we treated animals for 3 days post-surgery with DZX. Diazoxide diminished the increase in NLRP3 expression compared to the vehicle-treated group following axotomy in the hypoglossal nucleus, as represented by NLRP3 staining (Figure 6A) and quantitative analysis (8.49 ± 2.84 vs. 28.49 ± 5.98 %; axotomy + DZX vs. axotomy + vehicle; $p < 0.001$) (Figure 6B). Vehicle (DMSO) treatment did not have any significant effect on the axotomy-induced NLRP3 upregulation (Figure 6A,B).

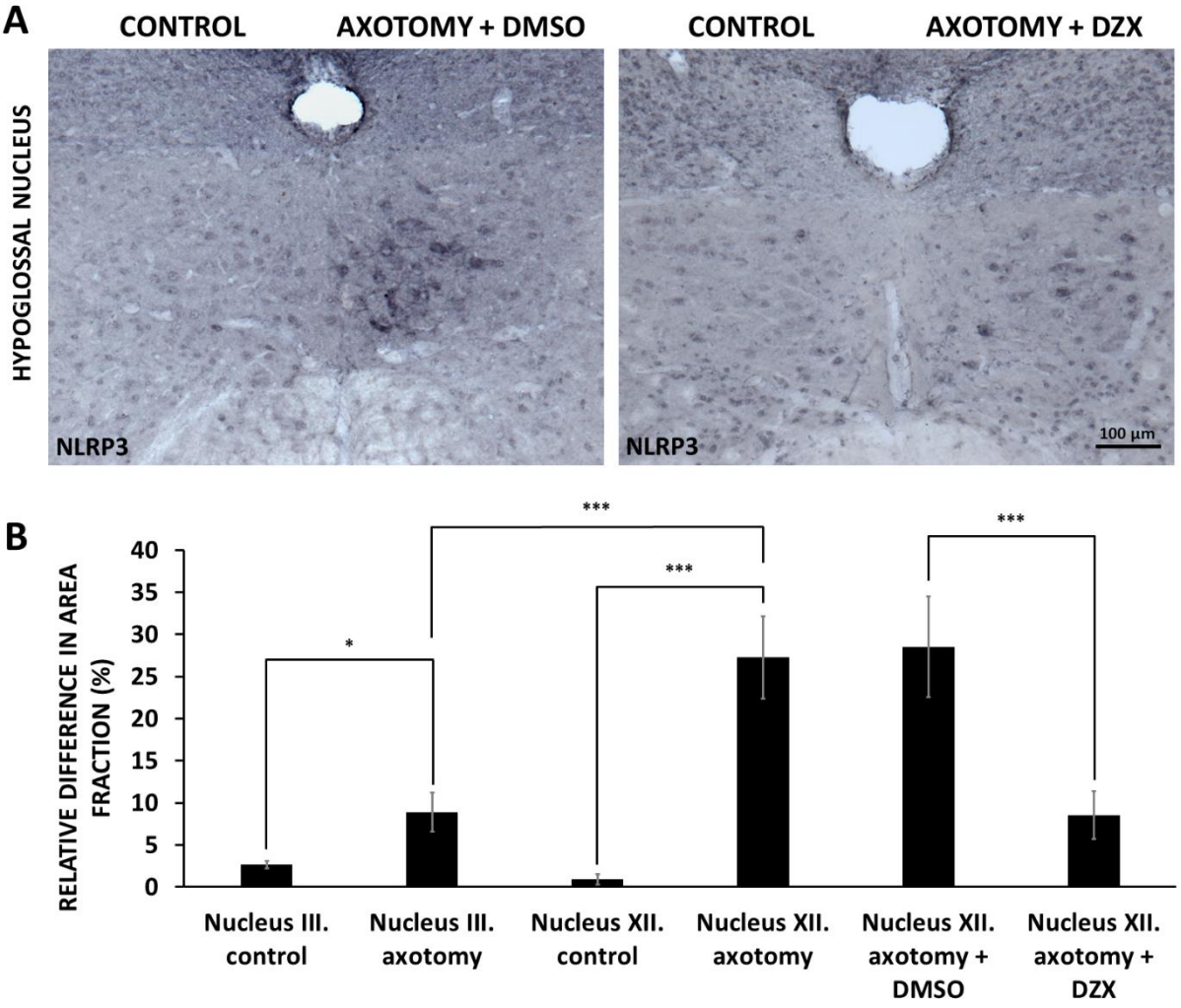

Figure 6. *Effect of diazoxide on NLRP3 protein expression in the hypoglossal nucleus. (A) Representative images of NLRP3 staining in the hypoglossal nucleus after axotomy and treatment with either vehicle (DMSO) or diazoxide (DMSO+DZX) for 3 days after surgery. (B) Quantitative analysis of NLRP3 protein expression in the oculomotor and in the hypoglossal nuclei after corresponding nerve axotomy. Hypoglossal nerve-axotomized mice were treated with either vehicle or vehicle + DZX. n = 5 animals/group. Graph represents the relative difference in the staining area fraction (average % ± SEM) of the operated side compared to the non-operated side of the nuclei (* = p < 0.05; *** = p < 0.001) (ANOVA with Fisher's LSD post-hoc). Scale bar: 100 µm.*

Effect of diazoxide on ramification and activation of microglial cells after hypoglossal axotomy

Following acute lesions of the central nervous system, microglial cells change their phenotype, migrate to the site of injury, reduce the complexity of their shape by retracting and thickening

their branches [79], which results in a more compact appearance of the immunostaining for microglial cells in the proximity of the injured neurons. Since microglial activation peaks around 5-7 days following axotomy [80,81], the effect of diazoxide on microgliosis was examined 7 days post-axotomy in the hypoglossal nucleus. Following axotomy, an elevated microglial reaction was observed on the operated side (1321 ± 146.69 arbitrary unit (a.u.); n = 3) (Figure 7A). In the DZX-treated group, the microglial activation decreased (933.15 ± 96.99 a.u.; n = 4) (Figure 7C) in comparison to the non-treated and DMSO-treated groups, but this change did not reach a significant level (p = 0.054) (Figure 7D).

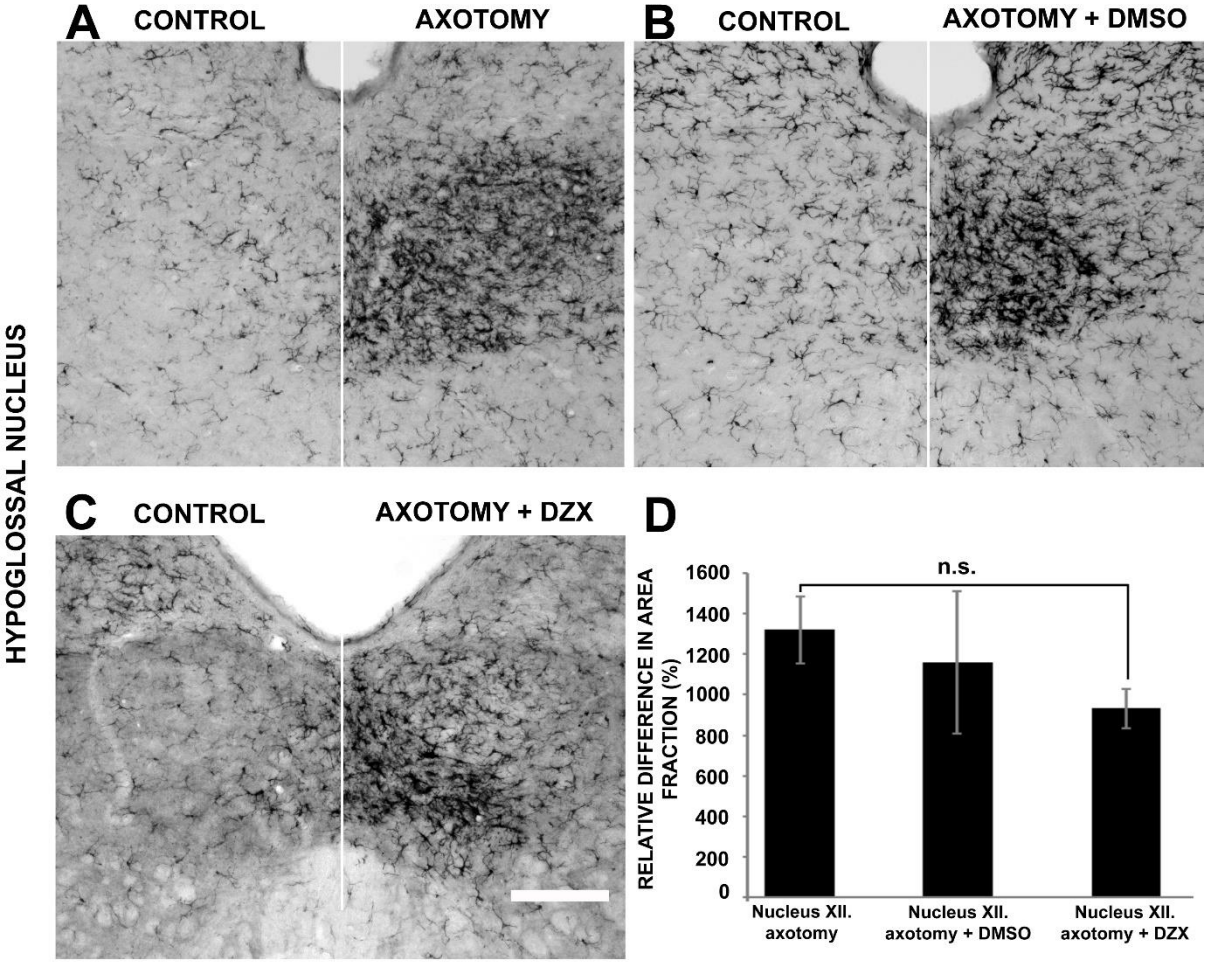

Figure 7. *Microglial activation in the hypoglossal nucleus after unilateral axotomy. (A) Representative images of microglial staining (Iba1) seven days after axotomy. When the axotomized animals received no treatment, intense microgliosis was observed on the operated side (right side) relative to the intact side (left side). (B) Representative images of the hypoglossal nucleus after axotomy + vehicle (DMSO) treatment. (C) Decreased microglial staining was observed in the DMSO+DZX-treated group following axotomy. (D) Qualitative analysis of microglial activation in the hypoglossal nucleus 7 days after axotomy. Each column*

represents the relative difference in area fraction compared to the contralateral (control) side of the nucleus. n = 3-4 animals/group. n.s.: non-significant (ANOVA with Fisher's LSD post-hoc). Scale bar: 100 μm.

To further clarify the effect of DZX on microglia, their morphology was also assessed in the hypoglossal nucleus. K-means-based Farthest-First cluster analysis on the output of multi-dimensional fractal analysis resulted in 2 separate cell clusters with a ramified-like (Figure 8A) and a bushy-like morphology (Figure 8B). 92.5 % of the examined microglial cells were sorted into cluster A on the control side of the hypoglossal nucleus (Figure 8C). This dramatically changed on the injured side, where all analyzed microglia were sorted into cluster B (Figure 8C). A similar change was observed in the DMSO-treated injured side, where 90 % of the microglia were categorized into cluster B (Figure 8C). DZX treatment could prevent this shift to cluster B phenotype (Fig. 8C).

Effect of diazoxide on motoneuronal survival and mitochondrial morphology

The effect of DZX on motoneuronal survival was also assessed by stereological cell counting in the hypoglossal nucleus to determine the neuroprotective effect of DZX. On day 7 after hypoglossal axotomy, we detected no motoneuronal loss based on the ratio of motoneurons compared to the control side. DMSO or DZX treatment had no significant effect on this ratio (axotomy only vs. axotomy+ DMSO vs. axotomy + DZX; 0.954 ± 0.05 vs. 1.04 ± 0.009 vs. 0.956 ± 0.02; n = 4 animals/group; $p > 0.05$; ANOVA with Fisher's LSD post-hoc). The present results of no detectable loss of motor neurons after axotomy in the hypoglossal nucleus are in accord with literature data describing similarly no loss of motor neurons in the facial nucleus of axotomized rats [82], or enucleated adult mice [76], in the same timeframe.

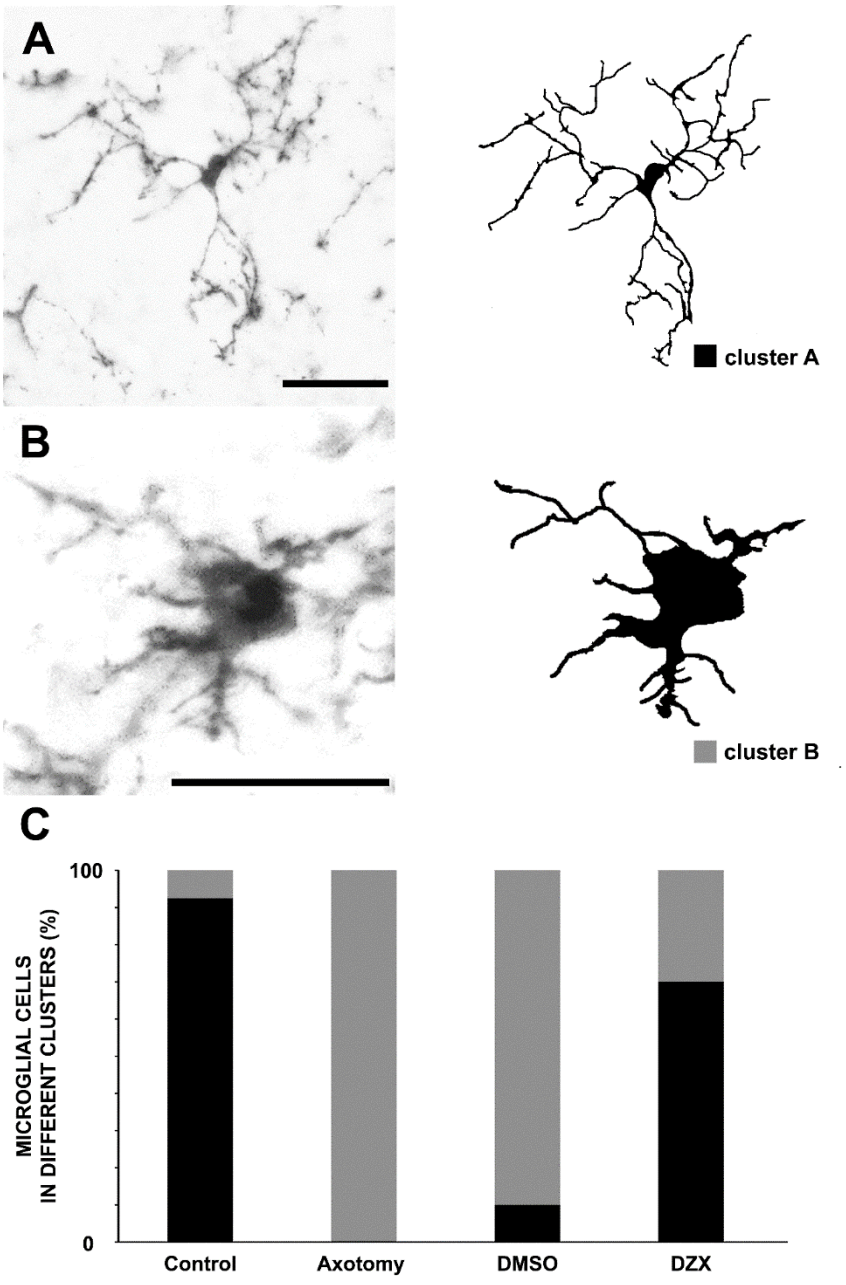

Figure 8. *Qualitative and quantitative changes in microglial morphology. (A) The ramified morphology of a single microglia cell with a small perinuclear area and long and branching processes from the control side is shown as a microscopic image and in a binarized form. (B) Activated microglial morphology is represented by the bushy-like shape with hypertrophic cytoplasm. (C) Quantitative evaluation was conducted on microglia, then cluster analysis was used to determine the ratio of microglial cells with distinctly different morphology. 92.5 % of all microglia from the control sides were classified into cluster A, represented by the ramified morphology on panel A. All microglia on the axotomized side without treatment were sorted into cluster B, with characteristic bushy-like shape represented on panel B. In the DMSO-treated group, 90 % of all examined microglia classified into cluster B. When treated with DZX, 70 % of the microglia on the injured side showed cluster A morphology, which represents the ramified-like phenotype (K-means based Farthest-First cluster analysis). Scale bar: 25 μm.*

Since DZX is known to modulate mitochondrial function, we conducted ultrastructural analysis of mitochondrial morphology to further examine the effect of DZX 4 days after axotomy. The

shape of mitochondria was more circular in the motoneurons of the control side of the hypoglossal nucleus (Figure 9A), but elongated mitochondria with ellipsoid shape and with an increased Feret's diameter could be observed in the motoneurons of the injured side of the hypoglossal nucleus (Figure 9B). DZX treatment (Figure 9C) restored this altered morphology and the Feret's diameter of these organelles in the hypoglossal motor neurons (Fig. 9E). The ratio of the Feret's diameter of the injured motoneuronal mitochondria compared to the control side was increased in the axotomized (1.27 ± 0.05) and in the vehicle (DMSO) control (1.29 ± 0.07) groups, implicating increased oxidative burden (Figure 9D). This elevation could be prevented with DZX treatment (axotomy only vs. axotomy + DZX: p = 0.00422). The morphology of microglial mitochondria was also examined, but none of the measured parameters showed significant changes (Figure 9E).

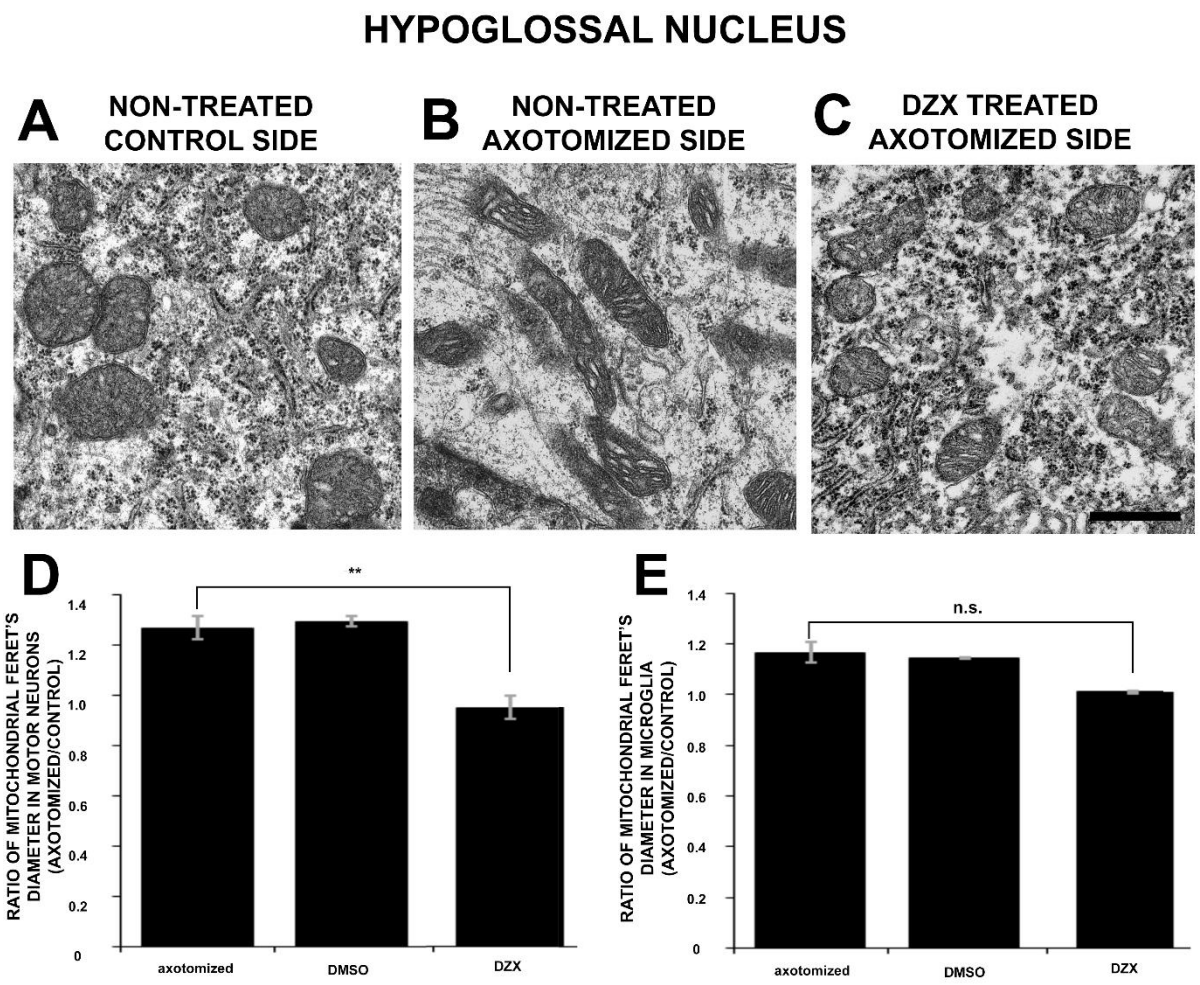

Figure 9. *Changes of the mitochondrial morphology of hypoglossal motoneurons and microglia 4 days after axotomy. (A) Representative EM images from the control hypoglossal nucleus without any treatment show round-shaped mitochondria with small Feret's diameter. (B) Motoneuronal cytoplasm from the non-treated operated side shows more ellipsoid*

*morphology with increased Feret's diameter. Besides the changes in the shape of these organelles, dilated cristae in the mitochondria could be noted on the operated side. (C) In the DZX-treated group, mitochondria regained their physiological morphology represented by their round shape and small Feret's diameter. (D-E) The ratio of mitochondrial Feret's diameter (injured/control side) was measured in motoneurons (D) and microglia (E). Mitochondria from axotomized animals without treatment, or vehicle (DMSO)-treated animals show an elevated Feret's diameter in motoneurons. A marginal, non-significant increase could be noted in microglia. DMSO+DZX treatment successfully reduced this elevation in the motoneurons, but this effect was not significant in microglia. **: $p < 0.01$ (ANOVA with Fisher's LSD post-hoc); n.s.: non-significant. n = 4 animals/group. Scale bar: 500 nm.*

NLRP3 expression in the spinal cord, dorsal root ganglion and sciatic nerve following sciatic nerve axotomy

Since sciatic nerve injury is a commonly accepted model of PNI and spinal cord motoneuron lesion, we also aimed to examined NLRP3 inflammasome activation following sciatic nerve axotomy. In the L4-L5 spinal cord segments NLRP3 protein expression was upregulated in the injured side at 1, 3 and 7 days post-axotomy (Figure 10A). Already on days 1 and 3 after axotomy, NLRP3 was observed in motoneurons, as revealed by ChAT and NLRP3 double staining (Figure 10B). The NLRP3 staining was either cytoplasmic or cytoplasmic and nuclear on the injury side, as observed in our previous experiments following hypoglossal axotomy. Notably, NLRP3 showed strong colocalization with the inflammasome adaptor protein ASC in the nuclei and later in the cytoplasm of motoneurons (Figure 10B), predicting inflammasome assembly. However, the two proteins showed partially distinct expression features, suggestive of possible inflammasome-independent functions as well. While NLRP3 was almost exclusively expressed in neurons in the first 3 days, on day 7 post-injury the NLRP3 signal appeared in GFAP- (Figure 10C) and Iba1-positive cells (Figure 10D) as well; however, without significant colocalization with ASC (Figure 10C-D). Nevertheless, NLRP3-positive microglia showed an activated phenotype, having their branches thickened and retracted, and localized in the proximity of the injured motoneurons (Figure 10D).

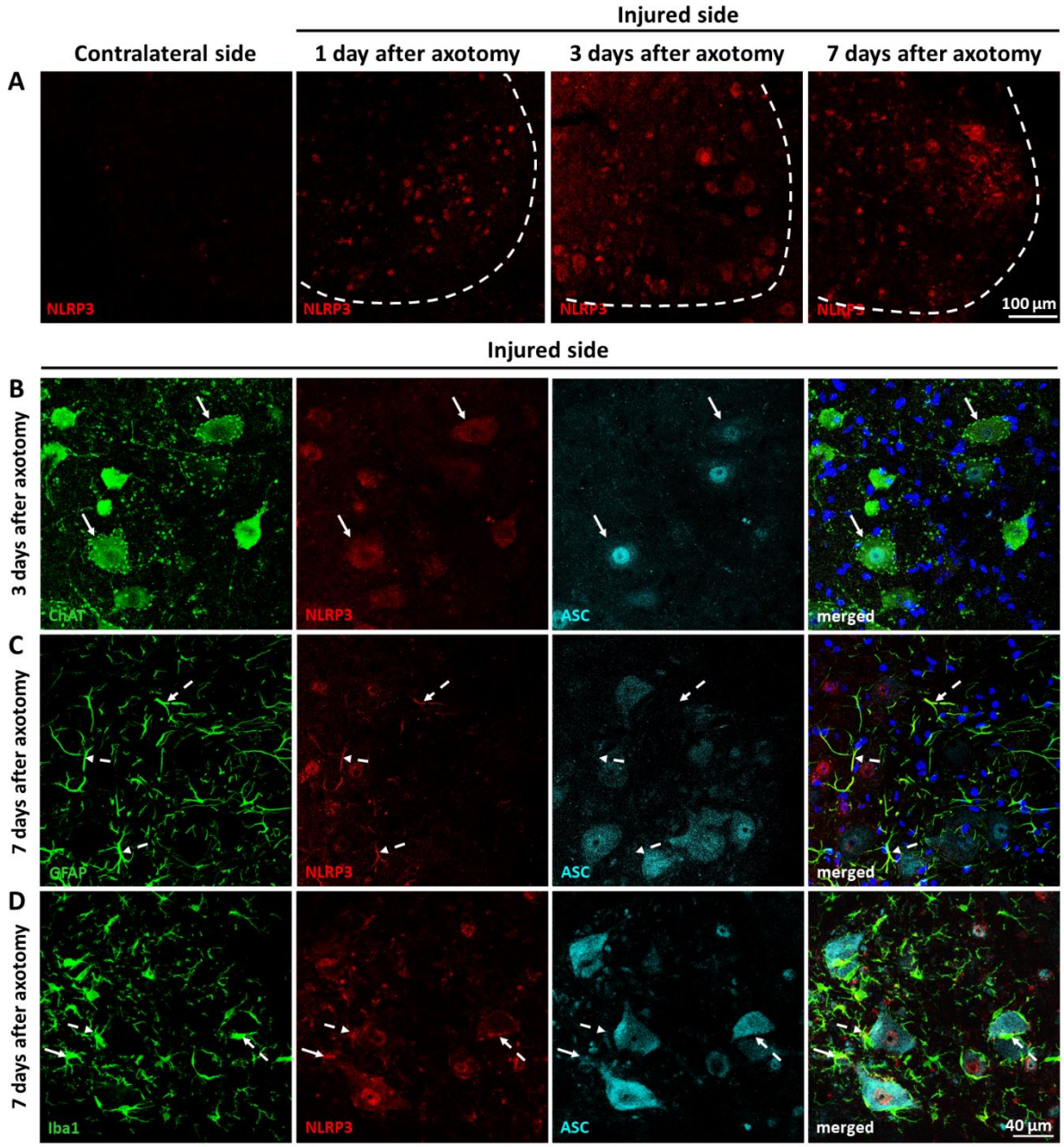

Figure 10. *Cellular localization of inflammasome components after sciatic nerve axotomy in the spinal cord. (A) NLRP3 expression in the ventral horn of the uninjured side, and of the injured side 1, 3 and 7 days following unilateral sciatic nerve axotomy. Dashed lines represent grey-white matter transition. (B) Colocalization of NLRP3 and ASC in motoneurons labeled with ChAT 3 days following nerve injury. Arrows point at NLRP3-ASC-positive motoneurons. (C) NLRP3 expression in GFAP-positive astroglia at 7 days following axotomy. Coexpression of NLRP3 and ASC was not observed in astroglia, as represented by dashed arrows. (D) Microglial NLRP3 around injured motoneurons 7 days after axotomy. NLRP3-positive microglia were mostly ASC-negative (dashed arrows); however, NLRP3-ASC-positive*

microglial cells were also sparsely observed (solid arrow). Scale bar: 100 µm (A) or 40 µm (B-D).

Importantly, NLRP3 and ASC were upregulated not only in the spinal cord, but also in Schwann cells (Figure 11) and in the microglia/macrophage population at the proximal end of the injured sciatic nerve (Figure 12), 3 days after the injury, accompanied by the increase of p75 and Iba1 expression as well (Figure 11-12). These results indicate that there is a parallel activation of NLRP3 in both the injured spinal cord and axotomized proximal nerve trunk, however with the involvement of different cell types.

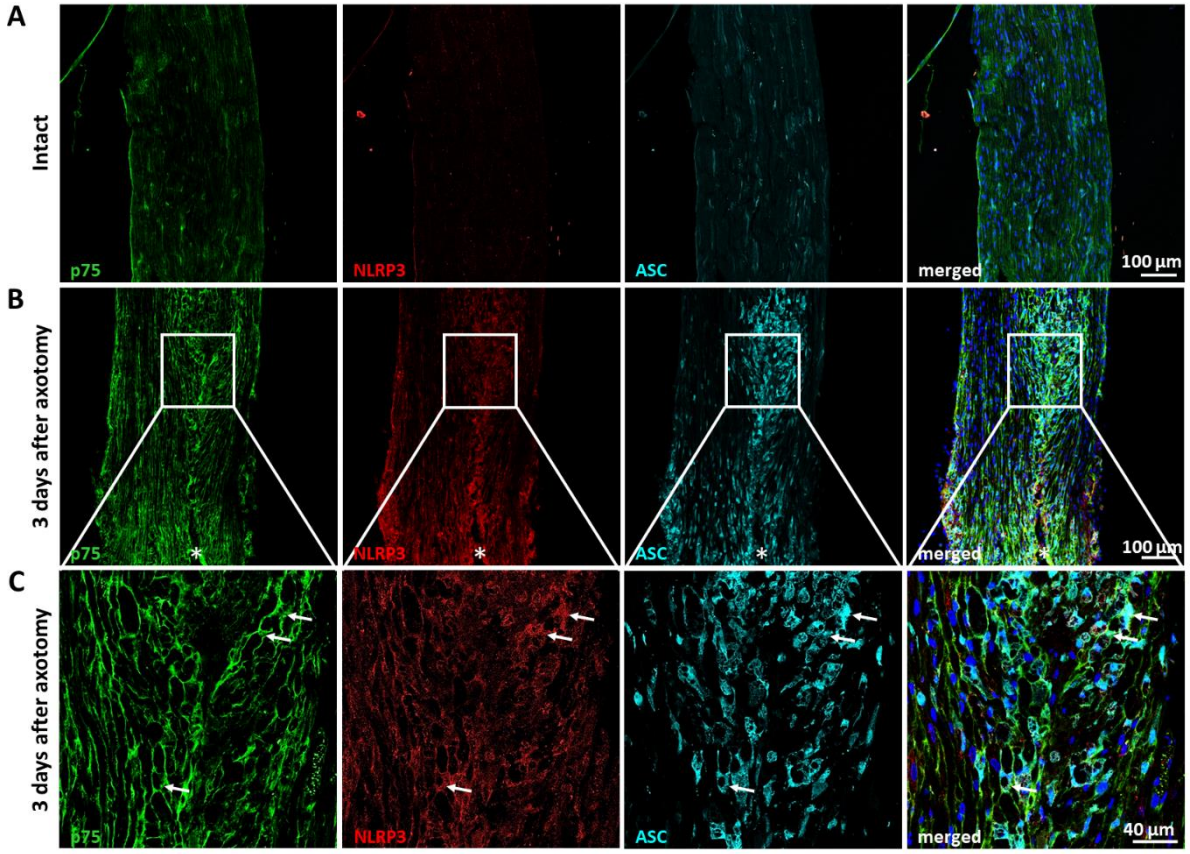

Figure 11. *NLRP3 and ASC expression in Schwann cells in the sciatic nerve. (A) Intact sciatic nerve from the control side, where minimal/negligible NLRP3 expression was observed. (B) Proximal end of the injured sciatic nerve 3 days post-axotomy. Asterisks indicate the point of transection. (C) Images on higher magnification from the proximal end of the injured sciatic nerve. Colocalization of NLRP3 and ASC in Schwann cells is indicated by solid arrows. Scale bar: 100 µm (A-B) or 40 µm (C).*

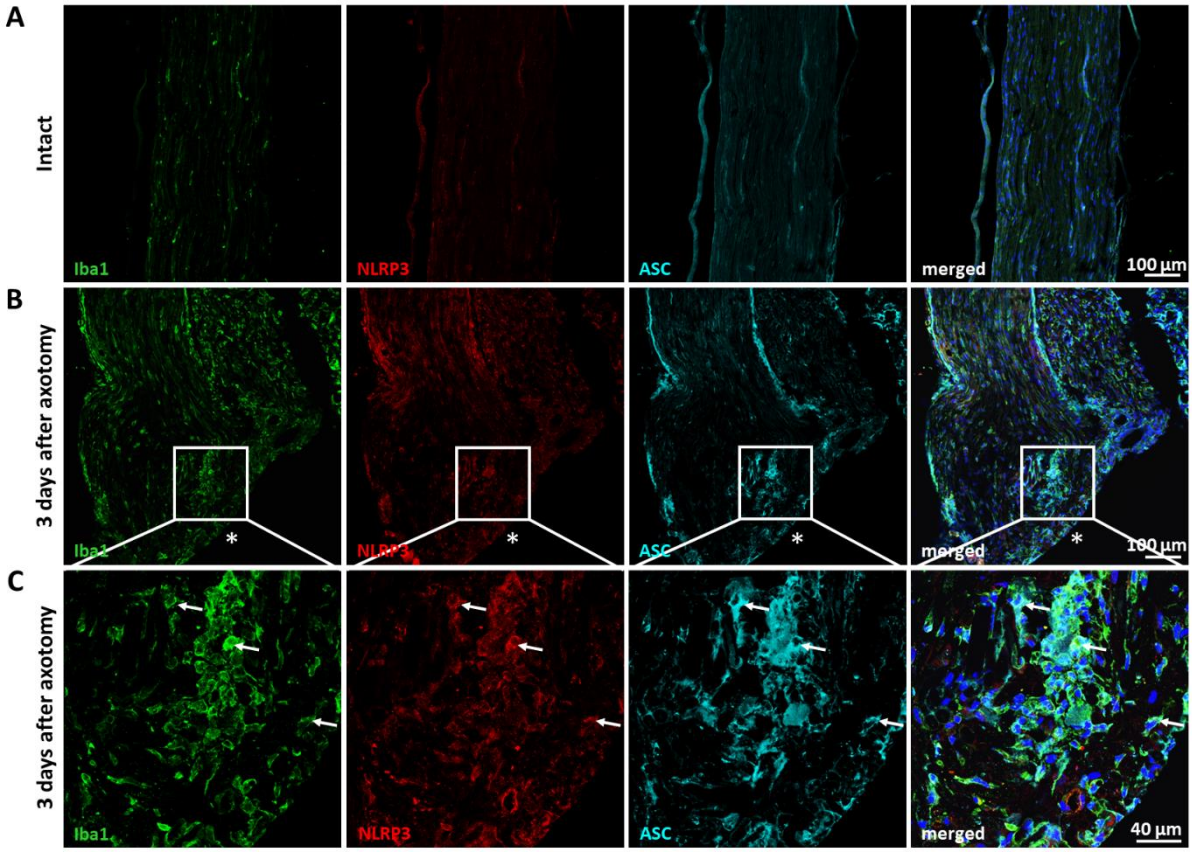

Figure 12. *NLRP3 and ASC expression in microglia/macrophages in the sciatic nerve. (A) Intact sciatic nerve from the contralateral side. (B) Proximal end of the injured sciatic nerve 3 days post-axotomy. Asterisks indicate the point of transection. (C) Higher magnification images from the proximal end of the injured sciatic nerve. Colocalization of NLRP3 and ASC in microglia/macrophages is indicated by solid arrows. Scale bar: 100 µm (A-B) or 40 µm (C).*

Even though this work primarily focused on the motor aspects of nerve injury, L4-L5 DRG has been assessed, as well. In the injured DRG, NLRP3 and ASC expression were similar to the control side, on day 3 post-axotomy (Figure 13), indicating that inflammasome activation either does not occur or arises at a later time point in sensory neurons of the DRG.

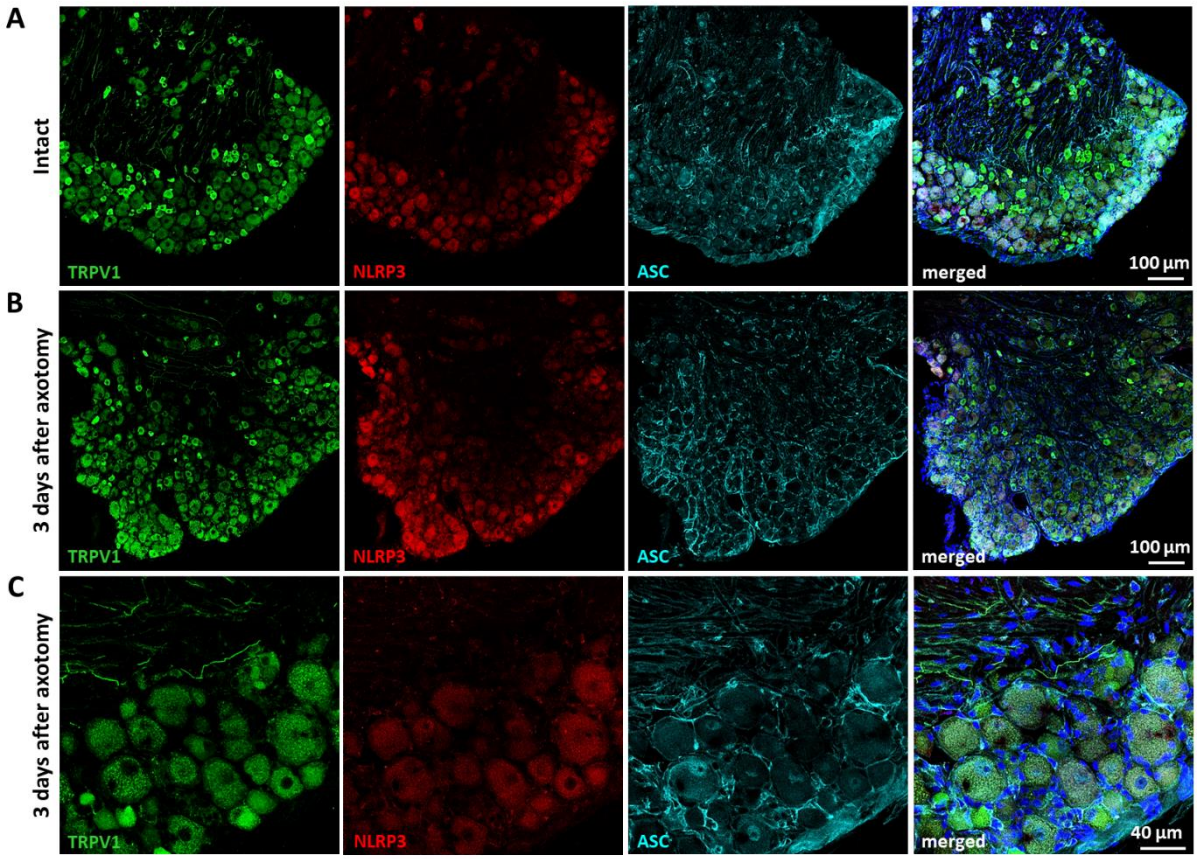

Figure 13. *NLRP3 and ASC expression in TRPV1-positive neurons in the DRG. (A) Expression of NLRP3 and ASC in the intact DRG from the control side. Note the strong basal expression of NLRP3 on the contralateral side. (B) NLRP3 and ASC expression in TRPV1-positive neurons in the injured DRG on day 3 post-axotomy. Injured TRPV-1 positive neurons show similar expression of NLRP3 to the contralateral (intact) side. (C) Higher magnification of NLRP3 and ASC expression in TRPV1-positive neurons. Scale bar: 100 µm (A-B) or 40 µm (C).*

Effect of NLRP3 inhibition on the microgliosis and astrogliosis in the spinal cord after sciatic nerve axotomy

The relationship between inflammasome activation and microglial activation was assessed, as well. Although early changes in microglial morphology were already observable on day 1, microgliosis became clearly detectable on the injured ventral horn of the L4-L5 spinal cord segments on day 3 post-axotomy (Figure 14A), when inflammasomal reaction was still restricted to motoneurons. Strong microglial reaction was present in the vehicle-treated (Figure 14A) animals, whereas the NLRP3 inhibitor MCC950 diminished the microglial reaction (Figure 14B), as revealed by quantitative analysis (18.2 ± 1.93 vs. 4.89 ± 1.04 %; axotomy + DMSO vs. axotomy + MCC950; $p < 0.001$).

Microgliosis was even higher on day 7 in the injured ventral horn of the vehicle-treated animals (Figure 14E); whereas administration of MCC950 for 3 days significantly decreased microglial reaction 7 days after the injury (Figure 14F-G) (28.33 ± 1.99 vs. 14.82 ± 1.39 %; axotomy + DMSO vs. axotomy + MCC950; $p < 0.001$).

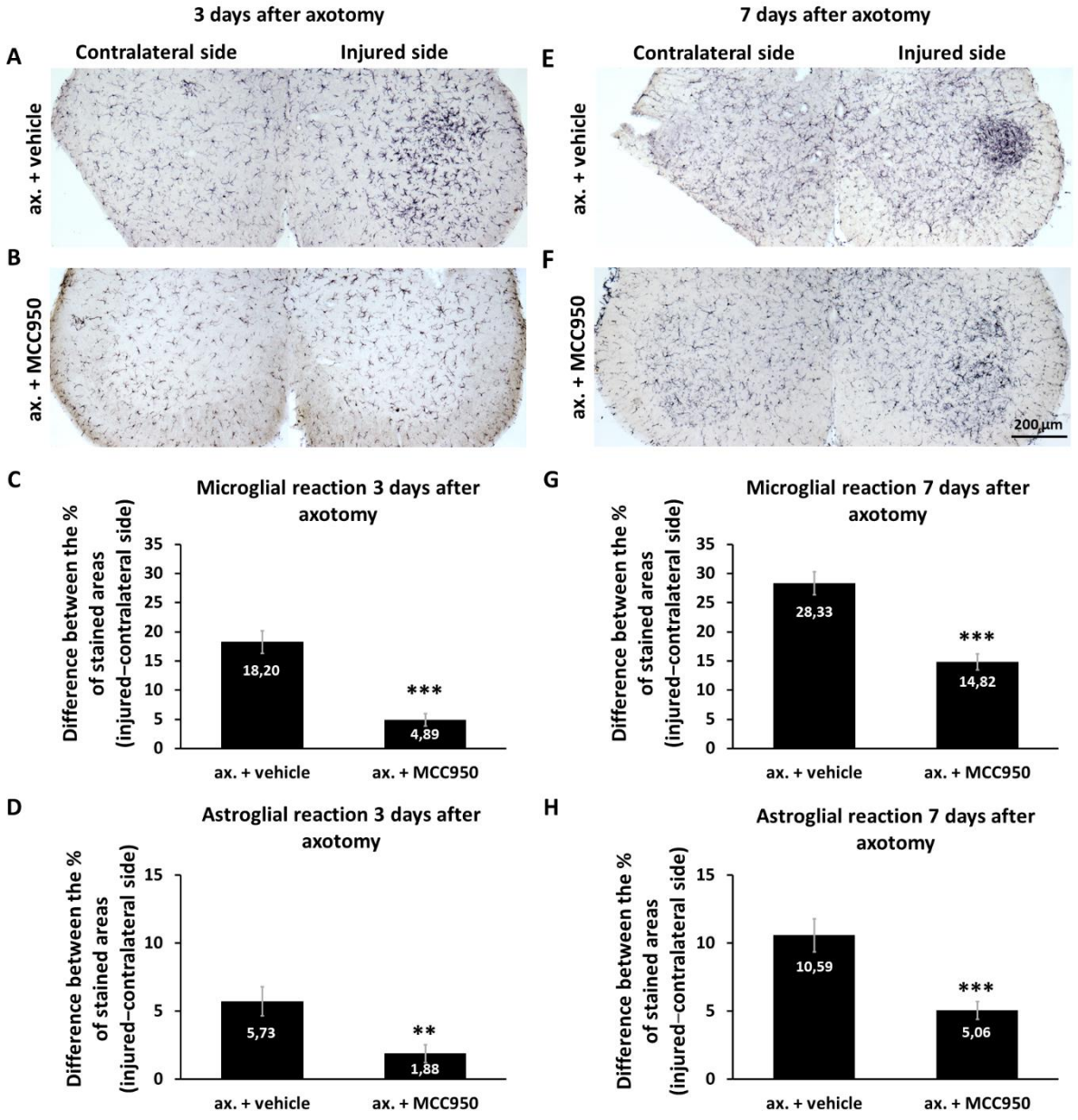

Figure 14. *Effect of MCC950 on microglial and astroglial activation in the L4-L5 spinal cord segments after sciatic nerve axotomy. (A-B) Microglial reaction, as assessed with Iba1 IHC, in the spinal cord 3 days post-axotomy. (C) Quantification of microglial reaction in the ventral horn 3 days following axotomy. Results are represented as the difference between the percentage of stained area on the injured and control sides. n = 4 animals/group; *** = p < 0.001 (Student's paired t-test). (D) Quantification of astrogliosis in the spinal cord*

*3 days after sciatic nerve axotomy. Columns represent the difference of the stained areas between the injured and control sides, average ± SEM. Mean values are shown on each column. n = 4 animals/group; ** = p < 0.01 (Student's paired t-test). (E-F) Microglial activation in the spinal cord 7 days post-axotomy. (G) Quantification of microglial reaction 7 days after sciatic axotomy. Results are represented as the difference of stained areas, similarly to (C-D). n = 4 animals/group. Significance marks are the same as for (C-D). Mean values are shown on all columns. Columns represent average ± SEM. (H) Quantification of astroglial reaction 7 days after the axotomy. Results are represented as the difference of stained areas, similarly to (C-D). n = 4 animals/group. Significance marks are the same as for (C-D). Mean values are shown on all columns. Columns represent average ± SEM. Ax.: axotomy. Scale bar: 200 μm.*

Since astrocyte activation in the injured ventral horn is known to contribute to nerve regeneration following PNI [83], the effect of MCC950 on astroglial reaction was assessed, as well. Astrogliosis was much weaker than microgliosis both on days 3 and 7, but could be reduced with MCC950 (Figure 14D,H), as revealed by quantitative analysis of astroglial reaction (3 days post-axotomy: 5.73 ± 1.06 vs. 1.88 ± 0.63 %; axotomy + DMSO vs. axotomy + MCC950; $p < 0.01$; 7 days post-axotomy: 10.59 ± 1.22 vs. 5.06 ± 0.64 %; axotomy + DMSO vs. axotomy + MCC950; $p < 0.001$).

In addition, administration of the NLRP3 inhibitor MCC950 in the first 3 days after axotomy reduced the extent of colocalization of Iba1 and NLRP3 on day 7 post-injury but did not have any diminishing effect on the weak colocalization of GFAP and NLRP3 (Figure 15A-B). Quantitatively, the ratio of colocalizing pixels on NLRP3-Iba1 staining was 50.50 ± 2.02 % (relative to the microglial area) in the axotomy + vehicle group, while it was reduced to 39.63 ± 0.88 % in the axotomy + MCC950 group ($p < 0.01$). No significant difference in the ratio of colocalizing pixels on the NLRP3-GFAP staining was observed (7.90 ± 1.94 vs. 8.50 ± 1.80 %; axotomy + vehicle vs. axotomy + MCC950; $p = 0.83$).

These results strongly suggest that inflammasome activation in motoneurons in the first days after nerve injury is the initiator of glial reaction in the spinal cord, although a parallel cascade cannot be definitely excluded.

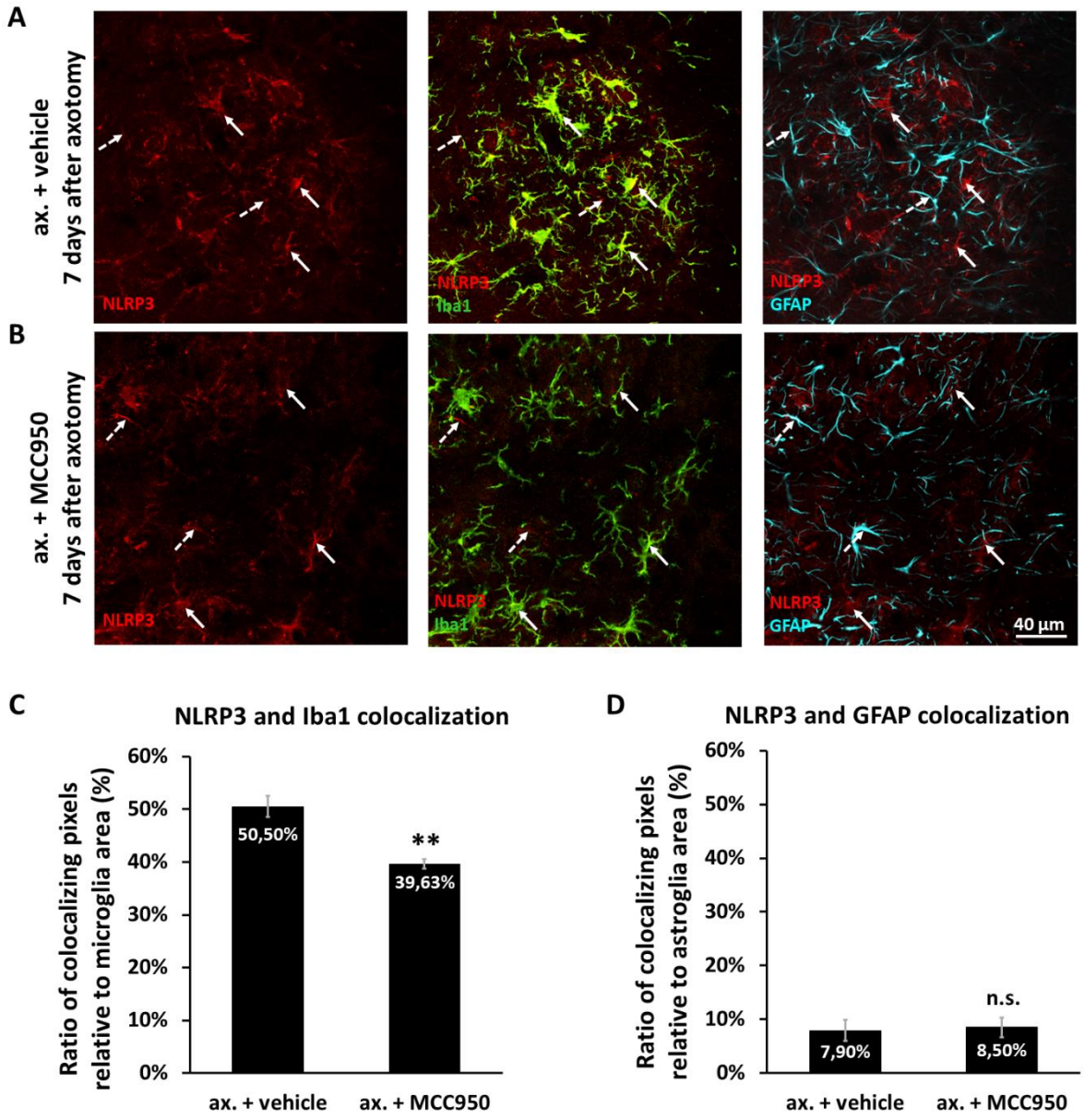

Figure 15. *NLRP3 upregulation in glial cells 7 days after peripheral nerve axotomy. (A-B) Colocalization of NLRP3 with the microglial marker Iba1 (solid arrows) and with astrocytes labeled with GFAP (dashed arrows) in the injured ventral horn 7 days after sciatic nerve axotomy in vehicle- (A) and MCC950-treated animals (B). (C) Quantification of NLRP3-Iba1 colocalization. Results represent the ratio of colocalizing pixels, relative to microglial area. n = 4 animals/group, ** = p < 0.01 (Student's paired t-test). (D) Quantification of NLRP3-GFAP colocalization. Graphs indicate the ratio of colocalizing pixels, relative to astroglial area. n = 4 animals/group, n.s.: non-significant (Student's paired t-test). Mean values are presented on all columns. Columns represent average ± SEM. Ax.: axotomy. Scale bar: 40 µm.*

Inhibition of inflammasome activation promotes neural regeneration

In order to investigate the possible functional consequences of neuronal inflammasome activation, sciatic nerve regeneration following sciatic nerve axotomy, and subsequent coaptation of nerve stumps with epineural sutures were assessed. We hypothesized that NLRP3 activation is induced, at least partly, through an extracellular ATP – purinergic receptor pathway, thus the effect of P2X4 receptor-specific inhibitor 5-BDBD was evaluated, in addition to the NLRP3 inflammasome inhibitor MCC950. Functional recovery, measured with the SFI method, was followed for 8 weeks in untreated animals and mice treated with vehicle, 5-BDBD or MCC950 in the first 3 days after axotomy and coaptation (when mainly neuronal inflammasome activation could be detected). In the untreated and vehicle-treated groups, a slow, but steady increase of the SFI was observed during the 8-week regenerative period (Figure 16A); furthermore, these results were comparable to what other authors published using suture-based coaptation [84]. In contrast, in animals treated with 5-BDBD or MCC950, a sharp initial recovery started on day 3 after coaptation, followed by a continuous improvement of SFI values (Figure 16A). From week 2 after coaptation, a significant difference was noted between treated and control groups until the end of the observation period. No significant difference was detected within the treated (5-BDBD, MCC950) and control (untreated, vehicle-treated) groups, *i.e.*, both the 5-BDBD and MCC950-treated groups performed equally well and DMSO treatment had no effect on functional recovery (Figure 16A).

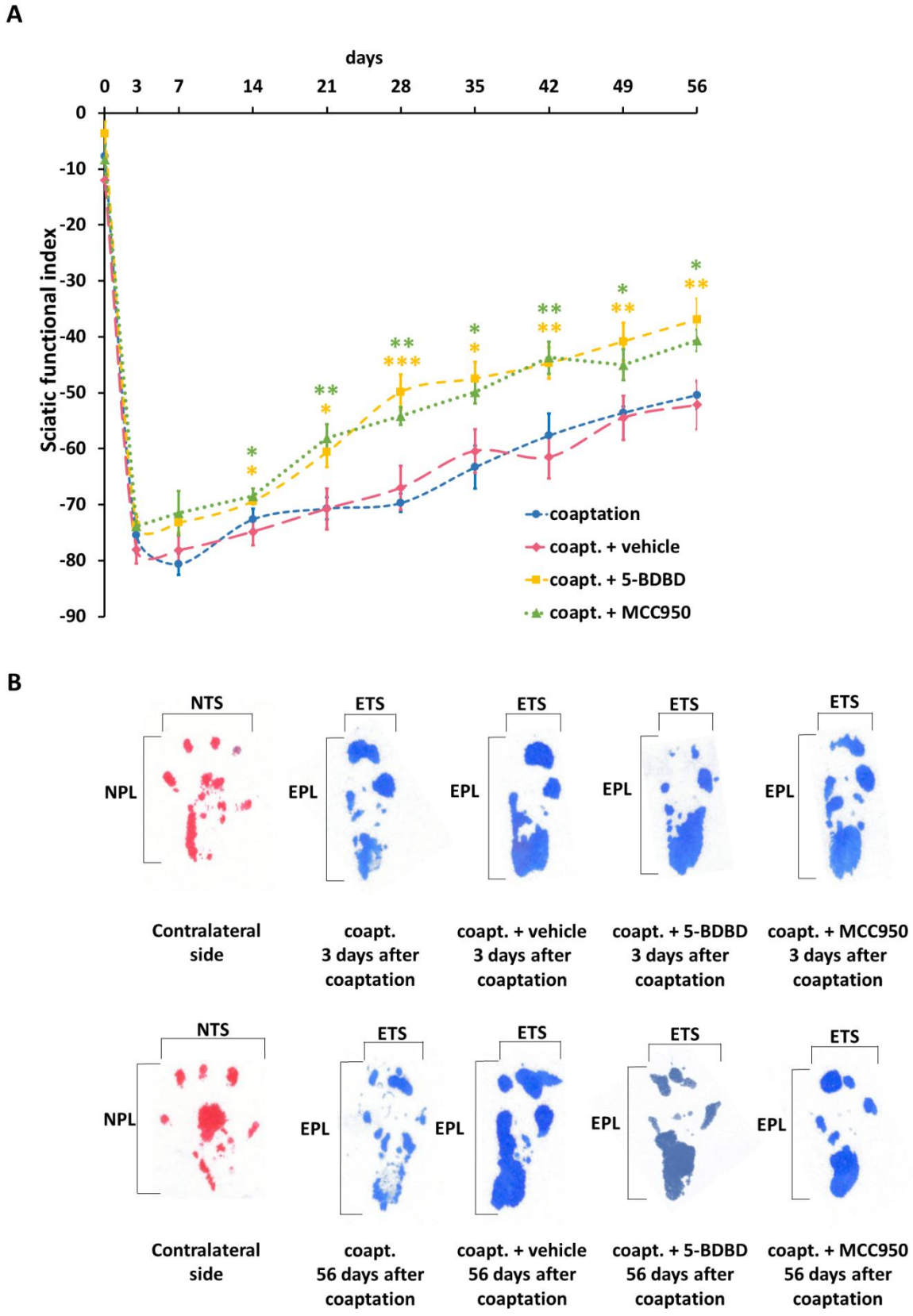

Figure 16. *Quantification of sciatic nerve regeneration with SFI measurement. (A) SFI scores over the 8-week regeneration period following axotomy and coaptation. Dots represent SFI*

*values at different time points, average ± SEM. No significant difference was observed between the control (coaptation only and coaptation + vehicle) groups. 5-BDBD and MCC950 treatment both resulted in a significant increase of the SFI compared to the vehicle-treated control group at 14 days and on. n = 5 animals/group; * = p < 0.05, ** = p < 0.01, *** = p < 0.001 (vs. coapt. + vehicle, ANOVA with Fisher's LSD post-hoc). (B) Representative images of mouse footprints 3 days (top panel) and 56 days (bottom panel) after coaptation. Coapt.: axotomy + coaptation, NTS: normal toe spread, NPL: normal paw length, ETS: experimental toe spread, EPL: experimental paw length.*

To quantify the number of motoneurons whose axons were able to grow through the coaptation site and regenerate into the distal sciatic nerve stump, retrograde labeling of regenerating motoneurons was performed. The sciatic nerve was cut distally from the coaptation point and FB crystals were applied for the assessment of axonal–somal connections based on retrograde transport of the dye. FB stained fewer motoneurons in the injured side of the spinal cord of untreated and vehicle-treated animals compared to the contralateral (intact) side (Figure 17B,C, compared to 17A), whereas 5-BDBD and MCC950 increased the number of FB-positive motoneurons in the spinal cord on the injured side (Figure 17D,E, compared to 17A). As expected from previous studies [85,86], less than 80 % of the total sciatic motoneuron pool were able to regenerate their axons into the distal stump in the untreated and vehicle-treated animals, while almost all axons of the sciatic motoneuron population grew beyond the coaptation site in animals treated with 5-BDBD or MCC950 (Figure 17F). As expected [87], axotomy only induced a slight reduction in the number of ChAT-positive motoneurons (to 90-95 %). Although the difference was not significant, both 5-BDBD and MCC950 were able to prevent motoneuron loss in the injured motor pool (Figure 17G).

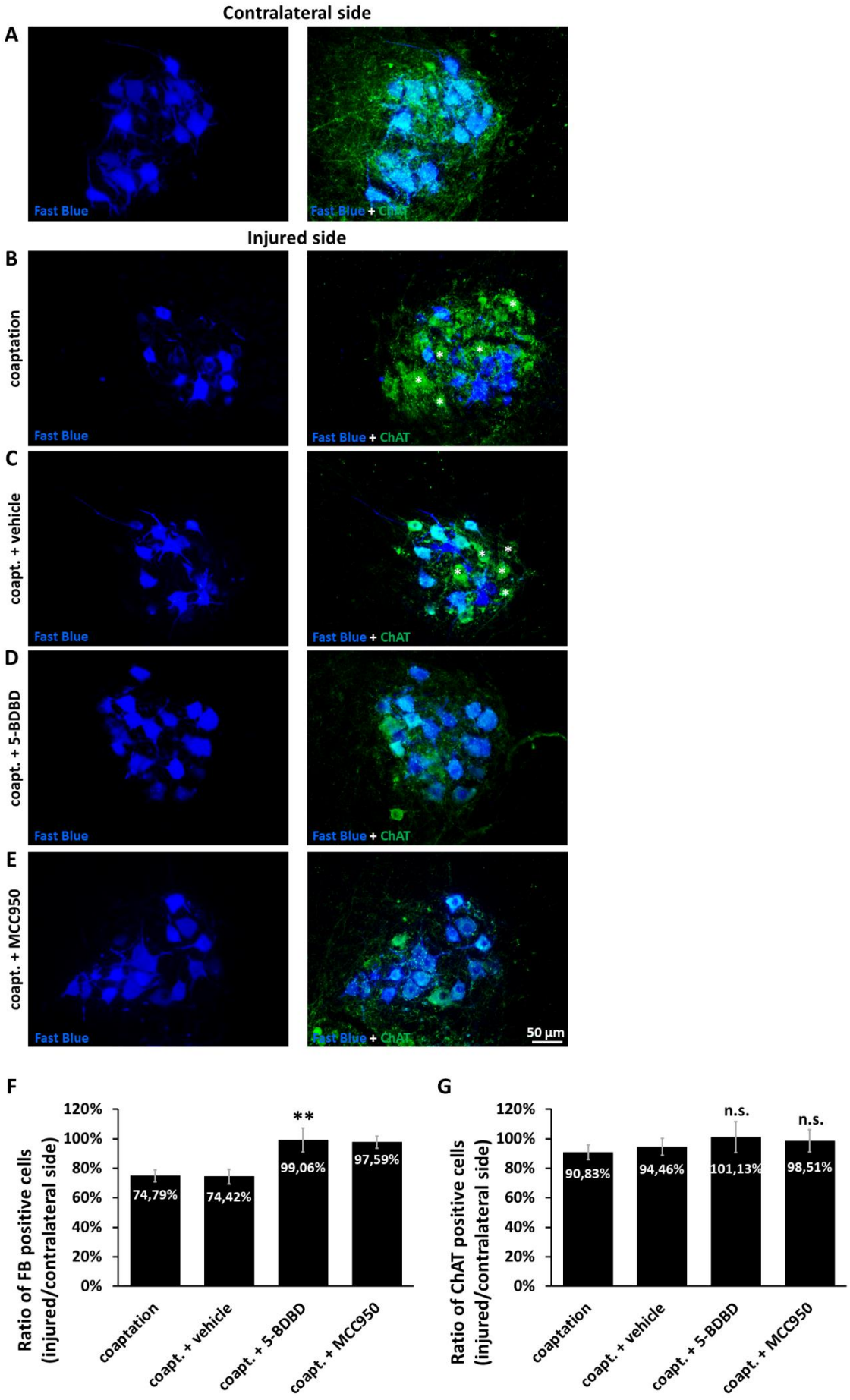
Contralateral side
A
Fast Blue
Fast Blue + ChAT
Injured side
B
coaptation
Fast Blue
Fast Blue + ChAT
C
coapt. + vehicle
Fast Blue
Fast Blue + ChAT
D
coapt. + 5-BDBD
Fast Blue
Fast Blue + ChAT
E
coapt. + MCC950
Fast Blue
Fast Blue + ChAT
50 µm
F
Ratio of FB positive cells (injured/contralateral side)
120%
100%
80%
60%
40%
20%
0%
74,79%
74,42%
99,06%
97,59%
**
coaptation
coapt. + vehicle
coapt. + 5-BDBD
coapt. + MCC950
G
Ratio of ChAT positive cells (injured/contralateral side)
120%
100%
80%
60%
40%
20%
0%
90,83%
94,46%
101,13%
98,51%
n.s.
n.s.
coaptation
coapt. + vehicle
coapt. + 5-BDBD
coapt. + MCC950

Figure 17. *Retrograde tracing of neuronal reinnervation following sciatic nerve injury. (A-E) Representative images showing the FB retrograde tracer signal combined with ChAT staining in the ventral horns from the contralateral side (A) and from the injured side (B-E) of lumbar spinal cord, 8 weeks after axotomy and coaptation. Asterisks indicate FB-negative motoneurons. In the untreated (coaptation only) (B) and vehicle-treated (C) groups, we observed partial reinnervation in the motoneuronal pool. Also note the increased ratio of FB-negative/ChAT-positive motoneurons. In the 5-BDBD- (D) and MCC950-treated (E) groups almost all the motoneurons are stained with FB, indicating higher ratio of reinnervation. (F) Quantification of the ratio of FB-positive motoneurons (injured/contralateral side), 8 weeks after sciatic nerve axotomy + coaptation. n = 5 animals/group. ** = p < 0.01 (ANOVA with Fisher's LSD post-hoc, compared to coapt. + vehicle). (G) Quantification of the ratio of ChAT-positive motoneurons 8 weeks after sciatic nerve axotomy + coaptation. n = 5 animals/group. n.s.: non-significant (ANOVA with Fisher's LSD post-hoc, compared to coapt. + vehicle). Coapt.: axotomy + coaptation. Mean values are presented on all columns. Columns represent average ± SEM. Scale bar: 50 μm.*

Retrograde labeling showed the extent of reinnervation at the endpoint of the investigated period of time. In order to study the early events of axonal regrowth including growth rate and number of regenerating axons, IF staining was performed using antibodies against neurofilament (NEFM, neurofilament medium polypeptide) and the Schwann cell marker p75 in the coaptation region of the sciatic nerve, 5 days after nerve axotomy and coaptation. In vehicle-treated animals, limited number of axons growing through the coaptation zone (Figure 18A) was observed at this relatively early time point following the axotomy + coaptation. Treatment of the animals with MCC950 increased the length and especially the number of regenerating axons (Figure 18B). These results support our expectations that morphological improvements precede the functional changes indicated by our SFI measurements. Quantification of the number and length of regrowing axons indicated a more than twofold improvement in regeneration in the MCC950-treated animals compared to vehicle-treated mice (10.45 ± 0.97 vs. 26.96 ± 2.74 a.u.; coapt. + vehicle vs. coapt. + MCC950; $p < 0.05$) (Figure 18C-D).

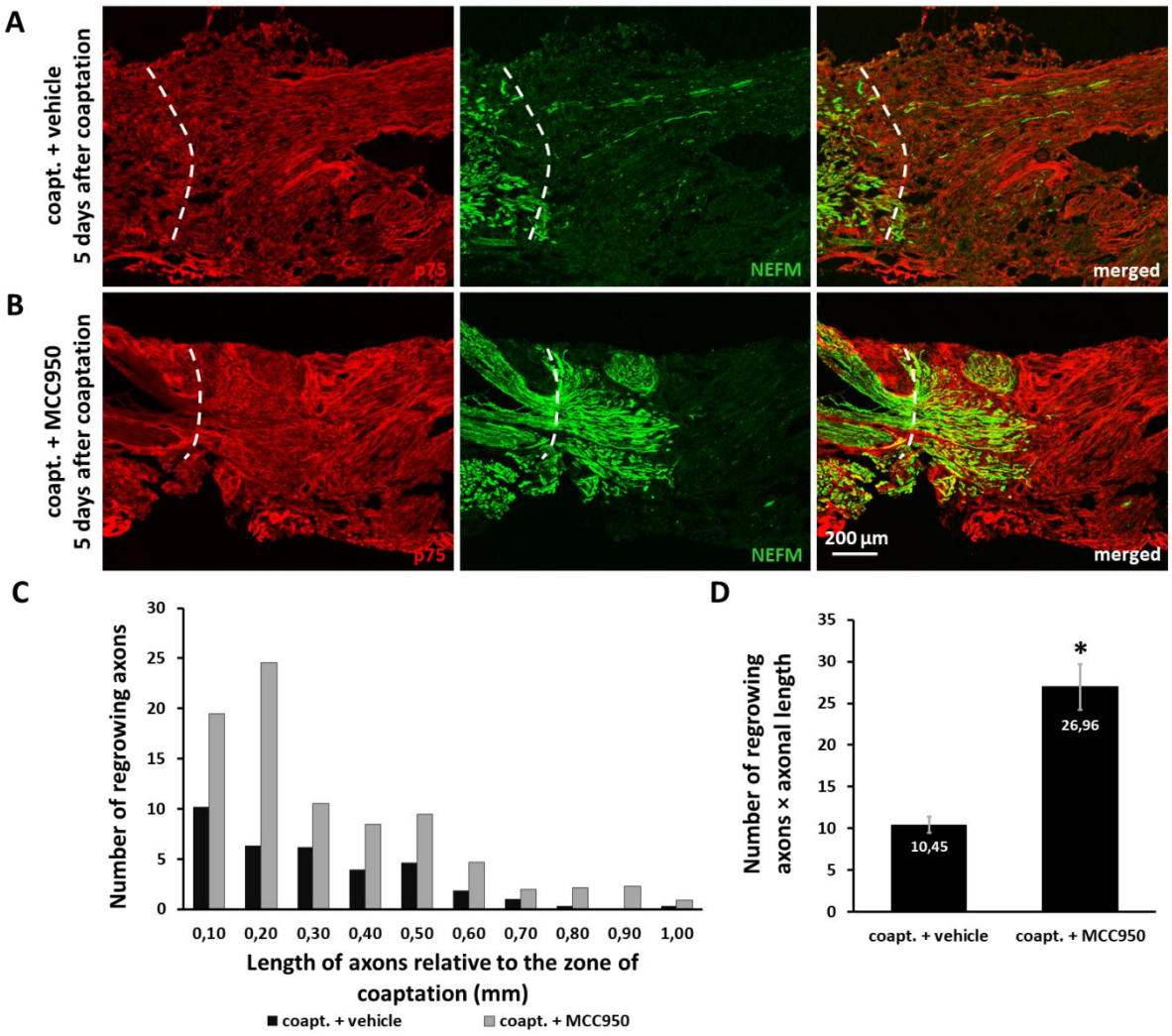

Figure 18. *Effect of MCC950 on axonal regrowth 5 days after sciatic nerve axotomy and coaptation. (A-B) Confocal images of injured sciatic nerves stained with the Schwann cell marker p75 and the axonal marker NEFM. In the vehicle-treated animals (A) a minimal number of short axons growing through the coaptation zone was observed. In comparison, in the MCC950-treated animals (B) a vast number of axons of various lengths have grown through the zone of coaptation at 5 days after axotomy + coaptation. (C) Quantification of regrowing axons 5 days after sciatic nerve injury. Columns represent the average number of regrowing axons and their distance relative to the zone of coaptation. (D) Graph represents the sum of regrowing axons derived as multiplication of axonal length and number of axons (i.e., area under the curve of graph (C)). Mean values are shown on columns. Columns represent average ± SEM. n = 3-4 animals/group; * = $p < 0.05$ (Student's paired t-test). Coapt.: axotomy + coaptation; a.u.: arbitrary unit. Scale bar: 200 µm.*

These results show that inhibition of NLRP3 activation in lumbar motoneurons not only hinders microgliosis but also facilitates axonal recovery after sciatic nerve injury.

Discussion

Crosstalk of the immune and nervous systems plays a crucial role in a large number of neuropathological conditions [88,89]. These include traumatic injuries both in the CNS and the PNS [23]; however, in peripheral nerve injuries, inflammatory reactions are generally studied only locally, while examination of the central immune response – apart from a few studies [81] – is either neglected or restricted to glial cells.

Peripheral nerve injury is indeed accompanied by strong local inflammatory reactions, which have been the subjects of extensive studies. These inflammatory reactions have conflicting consequences: if under control, may accelerate the regenerative processes, but overactivation can have opposite effects [23,90–92]. As a very potent inflammatory pathway, inflammasome activation was described to hinder recovery after sciatic nerve crush. In this model, NLRP3 inflammasome activation had a peak at 24 h in the injured nerve tissue, whereas absence of NLRP3 led to a faster recovery of the SFI [93]. However, another study questioned the activation of inflammasomes in sciatic nerve injury and concluded that priming of several inflammasome components is not followed by IL-1β cleavage, while NLRP6 contributes to the recovery independently of inflammasomes [94]. These conflicting studies show that the precise role and mechanism of PRR upregulation and inflammasome activation in acute neuronal injury is still largely undetermined, thus their potential application in pharmaceutical interventions is hindered.

In our experiments, axotomy of the hypoglossal or sciatic nerve, or target deprivation of the oculomotor nerve resulted in the increase of NLRP3 expression in the injured brain nuclei and lumbar spinal cord. Interestingly, this injury-induced upregulation of NLRP3 was significantly lower in the oculomotor nucleus, compared to the hypoglossal nucleus following axotomy. It is known that the oculomotor nucleus is considered to be resistant to degeneration in amyotrophic lateral sclerosis (ALS), thus such variability of the NLRP3 expression might be coupled to the improved ionic buffering capacity of oculomotor neurons, especially to their ability to control calcium accumulation in mitochondria [76] or differences in the expression of certain trophic factors in the hypoglossal nucleus [95].

Nevertheless, this study demonstrated that after acute lesion of the hypoglossal or sciatic nerves, motor neurons respond with a drastic upregulation of NLRP3. Previously, NLRP3 upregulation and inflammasome activation have already been acknowledged in certain CNS diseases [96]; however, microglia, the innate immune cells of the brain, have been primarily considered as resident cells involved in immunological processes of the CNS. Interestingly, in the applied axotomy model, motor neurons proved to initiate NLRP3 activation, while microglia were much less involved, despite their unequivocal role in the pathomechanism of neuronal injury-induced inflammation. Indeed, the role of other NLRs was not tested here, such as NLRP1 or absent in melanoma 2 (AIM2), which may also become upregulated in microglia or neurons as well, in response to axonal injury.

Although the present finding that NLRP3 was highly upregulated in neurons was somehow unexpected, neuronal NLRP3 upregulation and inflammasome activation have already been detected in a few pathological conditions. For example, ischemic stroke was shown to activate both NLRP1 and NLRP3 inflammasomes in neurons through nuclear factor kappa-light-chain-enhancer of activated B cells (NF-κB)- and mitogen-activated protein kinase-dependent mechanisms [97]. NLRP3 can also be a mediator of inflammatory pain, as chemical stimulation of the dura activated NLRP3 inflammasomes in C-type neurons in the trigeminal ganglion [98]. Furthermore, in the SOD1 (G93A) transgenic mice model of ALS, NLRP3 activation was predominantly detected in degenerating neurons of the anterodorsal thalamic nucleus [99]. Other studies also suggested activation of NLRP3 in neurons in injury and sterile inflammation [50,96]. Nevertheless, in TBI, a mechanical injury model, NLRP3 upregulation was approximately similar in neurons, astrocytes and microglia [100], while in spinal cord contusion injury, NLRP3 was primarily found in microglia and neurons [101]. However, to our best knowledge, inflammasome activation in the CNS after peripheral nerve injury has not been studied so far.

Under control conditions, a strong NLRP3 staining in the neuronal cell nuclei was observed. In response to nerve injury, NLRP3 was not only upregulated, but also translocated to the cytoplasm of motoneurons. Increased production of active IL-1β and IL-18 on the side of the injury suggests activation of inflammasomes, since cleavage of these cytokines is one of the best readout parameters of inflammasome activity [35,102,103]. Although the classical site of inflammasome assembly is the cytoplasm, a recent study revealed that six out of the 20 examined NLRs were detected in the nucleus as well. These include NLRP1, NLRP3, NLRP5, NLRP6, NLR family acidic transactivating domain (NLRA) and NLRC5 [104]. Although we

could clearly detect translocation of NLRP3 from the nucleus to the cytoplasm after nerve injury, a faint NLRP3 signal could still be detected in the nucleus, showing colocalization with ASC. Interestingly, in certain cases, inflammasomes can be activated in the nucleus as well, *e.g.*, nuclear activation of interferon gamma-inducible protein 16 (IFI16) inflammasome could be detected in endothelial cells during Kaposi sarcoma-associated herpesvirus infection [105]. In the nucleus, activated caspase-1 may have other substrates than pro-IL-1β and pro-IL-18, *e.g.*, sirtuin-1. Besides participating in the formation of inflammasomes, nuclear NLRs may have other functions as well, *e.g.*, NLRP3 is a transcriptional regulator in T helper type 2 cells and a repressor of regulatory T cell differentiation [106,107]. It is unknown, whether beyond serving as a receptor in inflammasomes, NLRP3 has any regulatory functions in neurons.

It was also observed that in the ventral horn of the lumbar spinal cord, NLRP3 expression can be clearly detected in microglia 7 days following sciatic axotomy. Interestingly, this suggests a biphasic inflammasome upregulation/activation, where neurons/motoneurons are the primary responders, followed by a late-onset NLRP3 increase in microglia. It was also shown that the inflammasome formation results in active IL-1β release, which can serve as a DAMP signal and initiate further inflammasome activation [38]. Consequently, it is reasonable to assume that the neuronal phase of inflammasome activation can initiate or contribute to the upregulation of NLRP3 in microglial cells. This is further supported by our finding that MCC950 treatment for 3 days (in the neuronal phase of NLRP3 activation) reduces microglial NLRP3 7 days after sciatic axotomy.

Several therapeutic approaches have proved that inhibition of the NLRP3 pathway could successfully prevent or slow down neuronal loss in neurodegenerative disorders [108–110]. Based on this, reduction of NLRP3 activation seems to be a promising point of intervention in acute injury conditions as well. First, it has been shown that DZX, an activator of the mitochondrial ATP-dependent K+ channel, could reduce the upregulation of NLRP3 following hypoglossal nerve axotomy. Furthermore, DZX treatment also prevented the injury-induced change in microglial morphology and could reduce mitochondrial swelling in motoneurons. Interestingly, such effect on microglial mitochondrial morphology was not observed. Since mitochondrial dysfunction has a pivotal role in initiation and activation of the NLRP3 inflammasome [57], the ability of DZX to reduce neuronal mitochondrial injury could be a major pathway in dampening NLRP3 upregulation following acute nerve injury.

Direct inhibition of NLRP3 inflammasome activation with MCC950 for 3 days after sciatic nerve axotomy improved the functional outcome, increased the ratio of reinnervating motoneurons in the spinal cord and enhanced axonal regrowth in the injured sciatic nerve. Besides these effects on neuronal regeneration, a reduction in spinal cord microglial activity was detected at 3 and 7 days after axotomy. Although it is a reasonable assumption that the improved neuronal regeneration is the result of the anti-inflammatory properties of MCC950, we cannot exclude alternative pathways acting directly on neuronal signaling. It was previously shown that MCC950 reduces neuronal apoptosis in spinal cord injury [111], however in our experiments axotomy did not lead to significant loss of motoneurons in the ventral horn, in concordance with previous findings.

Furthermore, we also aimed to characterize the mediators of central inflammasome activation in this peripheral injury model. Despite the low level of motoneuronal cell death, DAMPs are released and sensed by inflammasomal or associated receptors. Extracellular ATP is one of the first mediators of tissue damage and is an important activator of the NLRP3 inflammasome through the P2X7 and P2X4 receptors [112,113]. After inhibiting P2X4 receptors with 5-BDBD in the first three days following sciatic axotomy, we observed an improved functional outcome and axonal reinnervation. Under resting conditions, although present in microglia as well [114], P2X4 receptors are mainly expressed in neurons in the spinal cord [52]. Increased P2X4 immunoreactivity was found to characterize degenerating motoneurons in the ventral horn in a transgenic rodent model of ALS [115]. In this respect, motoneuronal response to axotomy resembles ALS-like degeneration, not only through the possible role of P2X4 in neuronal injury, but also through other features, such as neuronal activation of NLRP3 [99], low level of apoptotic cell death and recruitment of microglial cells.

In addition to the morphological aspects, our experiments also provide evidence of the functional benefit of inflammasome blockage (*i.e.*, axonal regrowth and sciatic reinnervation) and indicate that P2X4 receptor or the NLRP3 inflammasome may serve as potential therapeutic targets in peripheral nerve injury. Based on our results it can be hypothesized that spinal cord motoneurons are major players in inflammasome activation, however, the contribution of Schwann cells and microglia/macrophages to the propagation of local inflammation in the injured nerve cannot be excluded by using pharmacological inhibitors, since both 5-BDBD and MCC950 - although able to penetrate the blood-brain barrier and therefore target the CNS - exert their effect systemically. The role of central mechanisms is further supported by literature

data, indicating an opposite effect of peripheral P2X4 receptors, since overexpression of this receptor in Schwann cells was found to promote remyelination after nerve injury [116].

In conclusion, our proposed aims were completed as follows:

- it was proven that NLRP3 is upregulated in the injured motoneurons in response to peripheral nerve axotomy, and the inflammasome activation leads to the release of active IL-1β and IL-18, and microglial activation.
- it was demonstrated that direct inhibition of NLRP3 inflammasome activation with MCC950 after sciatic nerve axotomy enhanced functional recovery, accelerated axonal regrowth and increased the number of reinnervating motoneurons.
- the contribution of P2X4 receptors to inflammasome activation was proven through inhibition with 5-BDBD following sciatic nerve axotomy.
- it was shown that DZX treatment reduced NLRP3 upregulation through restoring mitochondrial morphology in motoneurons.
- based on our results we concluded that motoneurons seem to be the primary responders regarding inflammasome activation and can greatly contribute to the overactivation of inflammatory pathways, ultimately limiting their own regenerative capabilities.

Summary

Peripheral nerve injuries are accompanied by inflammatory reactions, over-activation of which may hinder recovery. Among pro-inflammatory pathways, inflammasomes are one of the most potent, leading to release of active IL-1β. Our aim was to understand how inflammasomes participate in central inflammatory reactions accompanying peripheral nerve injury.

Hypoglossal and sciatic nerve axotomy and target deprivation of the oculomotor nerve resulted in the upregulation of NLRP3 in the corresponding brain nuclei and the ventral horn of the lumbar spinal cord. Increased levels of IL-1β and IL-18 were detected in the axotomized hypoglossal nucleus, indicating inflammasome activation. Although glial cells are traditionally viewed as initiators of neuroinflammation, in this acute phase of inflammation, NLRP3 inflammasome activation was found exclusively in affected motoneurons. The upregulation of NLRP3 was also accompanied by its nucleo-cytoplasmic translocation in the injured motoneurons. Although at later time points the NLRP3 protein was upregulated in microglia too, no signs of inflammasome activation were detected in these cells. Inhibition of

inflammasome activation with MCC950 in motoneurons in the first 3 days after nerve injury hindered development of microgliosis in the spinal cord. Moreover, P2X4 or inflammasome inhibition in the acute phase significantly enhanced nerve regeneration on both the morphological and the functional levels. DZX treatment reduced upregulation of NLRP3, likely through restoring mitochondrial morphology in motoneurons.

Our results indicate that the central reaction initiated by sciatic nerve axotomy starts with inflammasome activation in the injured motoneurons, which triggers a complex inflammatory reaction and activation of microglia. Inhibition of neuronal inflammasome activation not only leads to a significant reduction of microgliosis but has a beneficial effect on the recovery as well.

Bibliography

1. Asplund M, Nilsson M, Jacobsson A, Holst H von. Incidence of Traumatic Peripheral Nerve Injuries and Amputations in Sweden between 1998 and 2006. Neuroepidemiology. 2009;32:217–28.

2. Li NY, Onor GI, Lemme NJ, Gil JA. Epidemiology of Peripheral Nerve Injuries in Sports, Exercise, and Recreation in the United States, 2009 – 2018. Phys Sportsmed. 2021;49:355–62.

3. Rayner MLD, Healy J, Phillips JB. Repurposing Small Molecules to Target PPAR-γ as New Therapies for Peripheral Nerve Injuries. Biomolecules. 2021;11:1301.

4. Miclescu A, Straatmann A, Gkatziani P, Butler S, Karlsten R, Gordh T. Chronic neuropathic pain after traumatic peripheral nerve injuries in the upper extremity: prevalence, demographic and surgical determinants, impact on health and on pain medication. Scand J Pain. 2019;20:95–108.

5. Fitzgerald M, McKelvey R. Nerve injury and neuropathic pain — A question of age. Exp Neurol. 2016;275:296–302.

6. Bergmeister KD, Große-Hartlage L, Daeschler SC, Rhodius P, Böcker A, Beyersdorff M, et al. Acute and long-term costs of 268 peripheral nerve injuries in the upper extremity. Plos One. 2020;15:e0229530.

7. Seddon HJ. Three types of nerve injury. Brain. 1943;66:237–88.

8. Sunderland S. A classification of peripheral nerve injuries producing loss of function. Brain J Neurol. 1951;74:491–516.

9. Menorca RMG, Fussell TS, Elfar JC. Peripheral Nerve Trauma: Mechanisms of Injury and Recovery. Hand Clin. 2013;29:317–30.

10. Huebner EA, Strittmatter SM. Axon Regeneration in the Peripheral and Central Nervous Systems. Results Probl Cell Differ. 2009;48:339–51.

11. Höke A. Mechanisms of Disease: what factors limit the success of peripheral nerve regeneration in humans? Nat Clin Pract Neurol.2006;2:448–54.

12. ElAbd R, Alabdulkarim A, AlSabah S, Hazan J, Alhalabi B, Thibaudeau S. Role of Electrical Stimulation in Peripheral Nerve Regeneration: A Systematic Review. Plast Reconstr Surg – Glob Open. 2022;10:e4115.

13. Elzinga K, Tyreman N, Ladak A, Savaryn B, Olson J, Gordon T. Brief electrical stimulation improves nerve regeneration after delayed repair in Sprague Dawley rats. Exp Neurol. 2015;269:142–53.

14. Grinsell D, Keating CP. Peripheral Nerve Reconstruction after Injury: A Review of Clinical and Experimental Therapies. BioMed Res Int. 2014;2014:698256.

15. Pfister BJ, Gordon T, Loverde JR, Kochar AS, Mackinnon SE, Cullen DK. Biomedical engineering strategies for peripheral nerve repair: surgical applications, state of the art, and future challenges. Crit Rev Biomed Eng. 2011;39:81–124.

16. Martini R, Willison H. Neuroinflammation in the peripheral nerve: Cause, modulator, or bystander in peripheral neuropathies? Glia. 2016;64:475–86.

17. Ydens E, Cauwels A, Asselbergh B, Goethals S, Peeraer L, Lornet G, et al. Acute injury in the peripheral nervous system triggers an alternative macrophage response. J Neuroinflammation. 2012;9:176.

18. Waller AV, Owen R. XX. Experiments on the section of the glossopharyngeal and hypoglossal nerves of the frog, and observations of the alterations produced thereby in the structure of their primitive fibres. Philos Trans R Soc Lond. 1850;140:423–9.

19. Shamash S, Reichert F, Rotshenker S. The cytokine network of Wallerian degeneration: tumor necrosis factor-alpha, interleukin-1alpha, and interleukin-1beta. J Neurosci. 2002;22:3052–60.

20. Kreutzberg GW. Microglia: a sensor for pathological events in the CNS. Trends Neurosci. 1996;19:312–8.

21. Buscemi L, Price M, Bezzi P, Hirt L. Spatio-temporal overview of neuroinflammation in an experimental mouse stroke model. Sci Rep. 2019;9:507.

22. DiSabato DJ, Quan N, Godbout JP. Neuroinflammation: the devil is in the details. J Neurochem. 2016;139 Suppl 2:136–53.

23. Mietto BS, Mostacada K, Martinez AMB. Neurotrauma and Inflammation: CNS and PNS Responses. Mediators Inflamm. 2015;2015:e251204.

24. Benowitz LI, Popovich PG. Inflammation and axon regeneration. Curr Opin Neurol. 2011;24:577–83.

25. Kaur P, Sharma S. Recent Advances in Pathophysiology of Traumatic Brain Injury. Curr Neuropharmacol. 2018;16:1224–38.

26. Bergold PJ. Treatment of traumatic brain injury with anti-inflammatory drugs. Exp Neurol. 2016;275 Pt 3:367–80.

27. Knight JB, Schott NJ, Kentor ML, Williams BA. Neurotoxicity Questions Regarding Common Peripheral Nerve Block Adjuvants in Combination with Local Anesthetics. Curr Opin Anaesthesiol. 2015;28:598–604.

28. Lee JI, Hur JM, You J, Lee DH. Functional recovery with histomorphometric analysis of nerves and muscles after combination treatment with erythropoietin and dexamethasone in acute peripheral nerve injury. Plos One. 2020;15:e0238208.

29. Madura T, Tomita K, Terenghi G. Ibuprofen improves functional outcome after axotomy and immediate repair in the peripheral nervous system. J Plast Reconstr Aesthetic Surg. 2011;64:1641–6.

30. Martinon F, Burns K, Tschopp J. The Inflammasome: A Molecular Platform Triggering Activation of Inflammatory Caspases and Processing of proIL-β. Mol Cell. 2002;10:417–26.

31. Conforti-Andreoni C, Ricciardi-Castagnoli P, Mortellaro A. The inflammasomes in health and disease: from genetics to molecular mechanisms of autoinflammation and beyond. Cell Mol Immunol. 2011;8:135–45.

32. Kanneganti T-D. The inflammasome: firing up innate immunity. Immunol Rev. 2015;265:1–5.

33. Gong T, Liu L, Jiang W, Zhou R. DAMP-sensing receptors in sterile inflammation and inflammatory diseases. Nat Rev Immunol. 2020;20:95–112.

34. Vénéreau E, Ceriotti C, Bianchi ME. DAMPs from Cell Death to New Life. Front Immunol. 2015;6:422.

35. Broz P, Dixit VM. Inflammasomes: mechanism of assembly, regulation and signalling. Nat Rev Immunol. 2016;16:407–20.

36. Prow NA, Irani DN. The inflammatory cytokine, interleukin-1 beta, mediates loss of astroglial glutamate transport and drives excitotoxic motor neuron injury in the spinal cord during acute viral encephalomyelitis. J Neurochem. 2008;105:1276–86.

37. Liu X, Nemeth DP, McKim DB, Zhu L, DiSabato DJ, Berdysz O, et al. Cell-Type-Specific Interleukin 1 Receptor 1 Signaling in the Brain Regulates Distinct Neuroimmune Activities. Immunity. 2019;50:317-333.e6.

38. Paik S, Kim JK, Silwal P, Sasakawa C, Jo E-K. An update on the regulatory mechanisms of NLRP3 inflammasome activation. Cell Mol Immunol. 2021;18:1141–60.

39. Shen H-H, Yang Y-X, Meng X, Luo X-Y, Li X-M, Shuai Z-W, et al. NLRP3: A promising therapeutic target for autoimmune diseases. Autoimmun Rev. 2018;17:694–702.

40. Grant R, Dixit V. Mechanisms of disease: inflammasome activation and the development of type 2 diabetes. Front Immunol. 2013;4:50.

41. Mészáros Á, Molnár K, Nógrádi B, Hernádi Z, Nyúl-Tóth Á, Wilhelm I, et al. Neurovascular Inflammaging in Health and Disease. Cells. 2020;9:1614.

42. Marchetti C. The NLRP3 Inflammasome as a Pharmacological Target. J Cardiovasc Pharmacol. 2019;74:285–96.

43. Zhang X, Xu A, Lv J, Zhang Q, Ran Y, Wei C, et al. Development of small molecule inhibitors targeting NLRP3 inflammasome pathway for inflammatory diseases. Eur J Med Chem. 2020;185:111822.

44. Caseley EA, Poulter JA, Rodrigues F, McDermott MF. Inflammasome inhibition under physiological and pharmacological conditions. Genes Immun. 2020;21:211–23.

45. Coll RC, Hill JR, Day CJ, Zamoshnikova A, Boucher D, Massey NL, et al. MCC950 directly targets the NLRP3 ATP-hydrolysis motif for inflammasome inhibition. Nat Chem Biol. 2019;15:556–9.

46. Jiao J, Zhao G, Wang Y, Ren P, Wu M. MCC950, a Selective Inhibitor of NLRP3 Inflammasome, Reduces the Inflammatory Response and Improves Neurological Outcomes in Mice Model of Spinal Cord Injury. Front Mol Biosci. 2020;7:37.

47. Ismael S, Nasoohi S, Ishrat T. MCC950, the Selective Inhibitor of Nucleotide Oligomerization Domain-Like Receptor Protein-3 Inflammasome, Protects Mice against Traumatic Brain Injury. J Neurotrauma. 2018;35:1294–303.

48. Luo Y, Lu J, Ruan W, Guo X, Chen S. MCC950 attenuated early brain injury by suppressing NLRP3 inflammasome after experimental SAH in rats. Brain Res Bull. 2019;146:320–6.

49. Rodrigues RJ, Tomé AR, Cunha RA. ATP as a multi-target danger signal in the brain. Front Neurosci. 2015;9:148.

50. Chen K, Zhang J, Zhang W, Zhang J, Yang J, Li K, et al. ATP-P2X4 signaling mediates NLRP3 inflammasome activation: a novel pathway of diabetic nephropathy. Int J Biochem Cell Biol. 2013;45:932–43.

51. Han SJ, Lovaszi M, Kim M, D'Agati V, Haskó G, Lee HT. P2X4 receptor exacerbates ischemic AKI and induces renal proximal tubular NLRP3 inflammasome signaling. FASEB J. 2020;34:5465–82.

52. de Rivero Vaccari JP, Bastien D, Yurcisin G, Pineau I, Dietrich WD, De Koninck Y, et al. P2X4 receptors influence inflammasome activation after spinal cord injury. J Neurosci. 2012;32:3058–66.

53. Sadatomi D, Nakashioya K, Mamiya S, Honda S, Kameyama Y, Yamamura Y, et al. Mitochondrial function is required for extracellular ATP-induced NLRP3 inflammasome activation. J Biochem. 2017;161:503–12.

54. Zhong Z, Liang S, Sanchez-Lopez E, He F, Shalapour S, Lin X, et al. New mitochondrial DNA synthesis enables NLRP3 inflammasome activation. Nature. 2018;560:198–203.

55. Elliott EI, Miller AN, Banoth B, Iyer SS, Stotland A, Weiss JP, et al. Cutting Edge: Mitochondrial Assembly of the NLRP3 Inflammasome Complex Is Initiated at Priming. J Immunol. 2018;200:3047–52.

56. Cauwels A, Rogge E, Vandendriessche B, Shiva S, Brouckaert P. Extracellular ATP drives systemic inflammation, tissue damage and mortality. Cell Death Dis. 2014;5:e1102–e1102.

57. Liu Q, Zhang D, Hu D, Zhou X, Zhou Y. The role of mitochondria in NLRP3 inflammasome activation. Mol Immunol. 2018;103:115–24.

58. Coetzee WA. Multiplicity of effectors of the cardioprotective agent, diazoxide. Pharmacol Ther. 2013;140:167–75.

59. Teshima Y, Akao M, Li RA, Chong TH, Baumgartner WA, Johnston MV, et al. Mitochondrial ATP-Sensitive Potassium Channel Activation Protects Cerebellar Granule Neurons From Apoptosis Induced by Oxidative Stress. Stroke. 2003;34:1796–802.

60. Domoki F, Bari F, Nagy K, Busija DW, Siklós L. Diazoxide prevents mitochondrial swelling and Ca2+ accumulation in CA1 pyramidal cells after cerebral ischemia in newborn pigs. Brain Res. 2004;1019:97–104.

61. Lei X, Lei L, Zhang Z, Cheng Y. Diazoxide inhibits of ER stress-mediated apoptosis during oxygen-glucose deprivation in vitro and cerebral ischemia-reperfusion in vivo. Mol Med Rep. 2018;17:8039–46.

62. Zhang L, Gao X, Yuan X, Dong H, Zhang Z, Wang S. Mitochondrial Calcium Uniporter Opener Spermine Attenuates the Cerebral Protection of Diazoxide through Apoptosis in Rats. J Stroke Cerebrovasc Dis. 2014;23:829–35.

63. Gong Z, Pan J, Shen Q, Li M, Peng Y. Mitochondrial dysfunction induces NLRP3 inflammasome activation during cerebral ischemia/reperfusion injury. J Neuroinflammation. 2018;15:242.

64. Fernández-Arjona M del M, Grondona JM, Granados-Durán P, Fernández-Llebrez P, López-Ávalos MD. Microglia Morphological Categorization in a Rat Model of Neuroinflammation by Hierarchical Cluster and Principal Components Analysis. Front Cell Neurosci. 2017;11:235

65. Karperien A, Ahammer H, Jelinek H. Quantitating the subtleties of microglial morphology with fractal analysis. Front Cell Neurosci. 2013;7:3.

66. Witten IH, Frank E. Data mining: practical machine learning tools and techniques with Java implementations. ACM SIGMOD Rec. 2002;31:76–7.

67. Hochbaum DS, Maass W. Approximation schemes for covering and packing problems in image processing and VLSI. J ACM. 1985;32:130–6.

68. Karnovsky M. A Formaldehyde-Glutaraldehyde Fixative of High Osmolality for Use in Electron Microscopy. J Cell Biol. 1964;27.

69. Errea O, Moreno B, Gonzalez-Franquesa A, Garcia-Roves PM, Villoslada P. The disruption of mitochondrial axonal transport is an early event in neuroinflammation. J Neuroinflammation. 2015;12:152.

70. Picard M, White K, Turnbull DM. Mitochondrial morphology, topology, and membrane interactions in skeletal muscle: a quantitative three-dimensional electron microscopy study. J Appl Physiol. 2013;114:161–71.

71. Federico M, Portiansky EL, Sommese L, Alvarado FJ, Blanco PG, Zanuzzi CN, et al. Calcium-calmodulin-dependent protein kinase mediates the intracellular signalling pathways of cardiac apoptosis in mice with impaired glucose tolerance. J Physiol. 2017;595:4089–108.

72. Demeter-Haludka V, Kovács M, Petrus A, Patai R, Muntean DM, Siklós L, et al. Examination of the Role of Mitochondrial Morphology and Function in the Cardioprotective Effect of Sodium Nitrite Administered 24 h Before Ischemia/Reperfusion Injury. Front Pharmacol. 2018;9:286.

73. Inserra MM, Bloch DA, Terris DJ. Functional indices for sciatic, peroneal, and posterior tibial nerve lesions in the mouse. Microsurgery. 1998;18:119–24.

74. Hayashi A, Moradzadeh A, Hunter DA, Kawamura DH, Puppala VK, Tung THH, et al. Retrograde Labeling in Peripheral Nerve Research: It Is Not All Black and White. J Reconstr Microsurg. 2007;23:381–9.

75. Faul F, Erdfelder E, Buchner A, Lang A-G. Statistical power analyses using G*Power 3.1: tests for correlation and regression analyses. Behav Res Methods. 2009;41:1149–60.

76. Obál I, Engelhardt JI, Siklós L. Axotomy induces contrasting changes in calcium and calcium-binding proteins in oculomotor and hypoglossal nuclei of Balb/c mice. J Comp Neurol. 2006;499:17–32.

77. McPhail LT, McBride CB, McGraw J, Steeves JD, Tetzlaff W. Axotomy abolishes NeuN expression in facial but not rubrospinal neurons. Exp Neurol. 2004;185:182–90.

78. Lams BE, Isacson O, Sofroniew MV. Loss of transmitter-associated enzyme staining following axotomy does not indicate death of brainstem cholinergic neurons. Brain Res. 1988;475:401–6.

79. Kettenmann H, Hanisch U-K, Noda M, Verkhratsky A. Physiology of Microglia. Physiol Rev. 2011;91:461–553.

80. Kawabori M, Yenari MA. The role of the microglia in acute CNS injury. Metab Brain Dis. 2015;30:381–92.

81. Paizs M, Patai R, Engelhardt JI, Katarova Z, Obal I, Siklos L. Axotomy Leads to Reduced Calcium Increase and Earlier Termination of CCL2 Release in Spinal Motoneurons with Upregulated Parvalbumin Followed by Decreased Neighboring Microglial Activation. CNS Neurol Disord Drug Targets. 2017;16:356–67.

82. Ichimiya T, Yamamoto S, Honda Y, Kikuchi R, Kohsaka S, Nakajima K. Functional down-regulation of axotomized rat facial motoneurons. Brain Res. 2013;1507:35–44.

83. Qian C, Tan D, Wang X, Li L, Wen J, Pan M, et al. Peripheral Nerve Injury-Induced Astrocyte Activation in Spinal Ventral Horn Contributes to Nerve Regeneration. Neural Plast. 2018;2018:e8561704.

84. Valero-Cabré A, Tsironis K, Skouras E, Navarro X, Neiss WF. Peripheral and Spinal Motor Reorganization after Nerve Injury and Repair. J Neurotrauma. 2004;21:95–108.

85. Brushart TM, Mesulam MM. Alteration in connections between muscle and anterior horn motoneurons after peripheral nerve repair. Science. 1980;208:603–5.

86. Wood MD, Kemp SWP, Weber C, Borschel GH, Gordon T. Outcome measures of peripheral nerve regeneration. Ann Anat Anz Off Organ Anat Ges. 2011;193:321–33.

87. Elliott JL, Snider WD. Axotomy-Induced Motor Neuron Death. In: Koliatsos VE, Ratan RR, editors. Cell Death Dis Nerv Syst. Totowa, NJ: Humana Press; 1999;p. 181–96.

88. Schwartz M, Deczkowska A. Neurological Disease as a Failure of Brain-Immune Crosstalk: The Multiple Faces of Neuroinflammation. Trends Immunol. 2016;37:668–79.

89. Trakhtenberg EF, Goldberg JL. Neuroimmune Communication. Science. American Association for the Advancement of Science; 2011;334:47–8.

90. Nadeau S, Filali M, Zhang J, Kerr BJ, Rivest S, Soulet D, et al. Functional Recovery after Peripheral Nerve Injury is Dependent on the Pro-Inflammatory Cytokines IL-1β and TNF: Implications for Neuropathic Pain. J Neurosci. 2011;31:12533–42.

91. Szepanowski F, Donaldson DM, Hartung H-P, Mausberg AK, Kleinschnitz C, Kieseier BC, et al. Dimethyl fumarate accelerates peripheral nerve regeneration via activation of the anti-inflammatory and cytoprotective Nrf2/HO-1 signaling pathway. Acta Neuropathol. 2017;133:489–91.

92. Hirschberg DL, Yoles E, Belkin M, Schwartz M. Inflammation after axonal injury has conflicting consequences for recovery of function: rescue of spared axons is impaired but regeneration is supported. J Neuroimmunol. 1994;50:9–16.

93. Cui M, Liang J, Xu D, Zhao L, Zhang X, Zhang L, et al. NLRP3 inflammasome is involved in nerve recovery after sciatic nerve injury. Int Immunopharmacol. 2020;84:106492.

94. Ydens E, Demon D, Lornet G, De Winter V, Timmerman V, Lamkanfi M, et al. Nlrp6 promotes recovery after peripheral nerve injury independently of inflammasomes. J Neuroinflammation. 2015;12:143.

95. Maugeri G, D'Amico AG, Morello G, Reglodi D, Cavallaro S, D'Agata V. Differential Vulnerability of Oculomotor Versus Hypoglossal Nucleus During ALS: Involvement of PACAP. Front Neurosci. 2020;14:805.

96. Voet S, Srinivasan S, Lamkanfi M, van Loo G. Inflammasomes in neuroinflammatory and neurodegenerative diseases. EMBO Mol Med. 2019;11:e10248.

97. Fann DY-W, Lim Y-A, Cheng Y-L, Lok K-Z, Chunduri P, Baik S-H, et al. Evidence that NF-κB and MAPK Signaling Promotes NLRP Inflammasome Activation in Neurons Following Ischemic Stroke. Mol Neurobiol. 2018;55:1082–96.

98. Chen L, Li X, Huang L, Wu Q, Chen L, Wan Q. Chemical stimulation of the intracranial dura activates NALP3 inflammasome in trigeminal ganglia neurons. Brain Res. 2014;1566:1–11.

99. Debye B, Schmülling L, Zhou L, Rune G, Beyer C, Johann S. Neurodegeneration and NLRP3 inflammasome expression in the anterior thalamus of SOD1(G93A) ALS mice. Brain Pathol. 2018;28:14–27.

100. Liu H-D, Li W, Chen Z-R, Hu Y-C, Zhang D-D, Shen W, et al. Expression of the NLRP3 inflammasome in cerebral cortex after traumatic brain injury in a rat model. Neurochem Res. 2013;38:2072–83.

101. Zendedel A, Johann S, Mehrabi S, Joghataei M-T, Hassanzadeh G, Kipp M, et al. Activation and Regulation of NLRP3 Inflammasome by Intrathecal Application of SDF-1a in a Spinal Cord Injury Model. Mol Neurobiol. 2016;53:3063–75.

102. He Y, Hara H, Núñez G. Mechanism and Regulation of NLRP3 Inflammasome Activation. Trends Biochem Sci. 2016;41:1012–21.

103. Zheng D, Liwinski T, Elinav E. Inflammasome activation and regulation: toward a better understanding of complex mechanisms. Cell Discov. 2020;6:36.

104. Wang L, Fu H, Nanayakkara G, Li Y, Shao Y, Johnson C, et al. Novel extracellular and nuclear caspase-1 and inflammasomes propagate inflammation and regulate gene expression: a comprehensive database mining study. J Hematol Oncol. 2016;9:122.

105. Kerur N, Veettil MV, Sharma-Walia N, Bottero V, Sadagopan S, Otageri P, et al. IFI16 acts as a nuclear pathogen sensor to induce the inflammasome in response to Kaposi Sarcoma-associated herpesvirus infection. Cell Host Microbe. 2011;9:363–75.

106. Bruchard M, Rebé C, Derangère V, Togbé D, Ryffel B, Boidot R, et al. The receptor NLRP3 is a transcriptional regulator of TH2 differentiation. Nat Immunol. 2015;16:859–70.

107. Park S-H, Ham S, Lee A, Möller A, Kim TS. NLRP3 negatively regulates Treg differentiation through Kpna2-mediated nuclear translocation. J Biol Chem. 2019;294:17951–61.

108. Dempsey C, Rubio Araiz A, Bryson KJ, Finucane O, Larkin C, Mills EL, et al. Inhibiting the NLRP3 inflammasome with MCC950 promotes non-phlogistic clearance of amyloid-β and cognitive function in APP/PS1 mice. Brain Behav Immun. 2017;61:306–16.

109. Gordon R, Albornoz EA, Christie DC, Langley MR, Kumar V, Mantovani S, et al. Inflammasome inhibition prevents α-synuclein pathology and dopaminergic neurodegeneration in mice. Sci Transl Med. 2018;10:eaah4066.

110. Zhou Y, Lu M, Du R-H, Qiao C, Jiang C-Y, Zhang K-Z, et al. MicroRNA-7 targets Nod-like receptor protein 3 inflammasome to modulate neuroinflammation in the pathogenesis of Parkinson's disease. Mol Neurodegener. 2016;11:28.

111. He N, Zheng X, He T, Shen G, Wang K, Hu J, et al. MCC950 Reduces Neuronal Apoptosis in Spinal Cord Injury in Mice. CNS Neurol Disord Drug Targets. 2021;20:298–308.

112. Kanellopoulos JM, Almeida-da-Silva CLC, Rüütel Boudinot S, Ojcius DM. Structural and Functional Features of the P2X4 Receptor: An Immunological Perspective. Front Immunol. 2021;12:852.

113. Cassel SL, Sutterwala FS. Sterile inflammatory responses mediated by the NLRP3 inflammasome. Eur J Immunol. 2010;40:607–11.

114. Duveau A, Bertin E, Boué-Grabot E. Implication of Neuronal Versus Microglial P2X4 Receptors in Central Nervous System Disorders. Neurosci Bull. 2020;36:1327–43.

115. Casanovas A, Hernández S, Tarabal O, Rosselló J, Esquerda JE. Strong P2X4 purinergic receptor-like immunoreactivity is selectively associated with degenerating neurons in transgenic rodent models of amyotrophic lateral sclerosis. J Comp Neurol. 2008;506:75–92.

116. Su W-F, Wu F, Jin Z-H, Gu Y, Chen Y-T, Fei Y, et al. Overexpression of P2X4 receptor in Schwann cells promotes motor and sensory functional recovery and remyelination via BDNF secretion after nerve injury. Glia. 2019;67:78–90.

Acknowledgements

Foremost I would like to express my gratitude to my supervisors, Dr. László Siklós and Dr. Roland Patai (Neuronal Plasticity Research Group, Institute of Biophysics, Biological Research Centre) for the mentorship, support, and guidance throughout my doctoral work.

I would like to thank Dr. István Krizbai and Dr. Imola Wilhelm (Neurovascular Unit Research Group, Institute of Biophysics, Biological Research Centre) for their valuable contributions and for enabling our collaborative work.

I would like to express my special thanks to Dr. Antal Nógrádi (Laboratory of Neural Regeneration, Department of Anatomy, Histology and Embryology, Faculty of Medicine, University of Szeged) not only for his professional advice, but also for encouraging and motivating me to pursue my passion.

I am grateful for the kind support of Dr. Péter Klivényi (Department of Neurology, Albert Szent-Györgyi Health Centre, University of Szeged).

I am grateful for all the support and work of the members of the Laboratory of Neuronal Regeneration, Neuronal Plasticity and Neurovascular Unit Research Groups, especially Dr. Kinga Mészáros-Molnár, Rebeka Kristóf, Dr. Ádám Nyúl-Tóth, Dr. Krisztián Pajer and Erika Bánfiné Rácz. Without their professional help, teamwork and the inspiring and friendly atmosphere they created, this dissertation would not have been possible to write.

I would like to express my special thanks to my fiancée, family, and friends for their support, tolerance, and love. This accomplishment is just as much theirs as it is mine.

This work was financially supported by the National Research, Development and Innovation Office through the GINOP-2.3.2-15-2016-00001, GINOP-2.3.2-15-2016-00034, GINOP-2.3.2-15-2016-00020, FK-124114, K-135425, K-135475 and TKP2021-EGA-09 programs, the ÚNKP-18-2-I-SZTE-84, ÚNKP-19-2-SZTE-92 and ÚNKP-20-2-SZTE-68 New National Excellence Program of the Ministry for Innovation and Technology of Hungary, the ELKH SA-73/2021 program and the Szeged Scientists Academy under the sponsorship of the Hungarian Ministry of Human Capacities (FEIF/433-4/2020-ITM_SZERZ). Support of UEFISCDI (Executive Agency for Higher Education, Research, Development and Innovation Funding, PN-III-P1-1.1-TE-2019-1302 and PN-III-P4-ID-PCE-2020-1529) is also acknowledged.